chemistry

MDPI

Article

Structural and Magnetic Analysis of a Family of Structurally Related Iron(III)-Oxo Clusters of Metal Nuclearity Fe_8, $Fe_{12}Ca_4$, and $Fe_{12}La_4$ †

Alok P. Singh [1], ChristiAnna L. Brantley [1], Kenneth Hong Kit Lee [1], Khalil A. Abboud [1], Juan E. Peralta [2] and George Christou [1,*]

[1] Department of Chemistry, University of Florida, Gainesville, FL 32611, USA
[2] Department of Physics and Science of Advanced Materials, Central Michigan University, Mount Pleasant, MI 48859, USA
* Correspondence: christou@chem.ufl.edu; Tel.: +1-352-392-8314
† Dedicated to Prof. Spyros P. Perlepes on the occasion of his 70th birthday: A wonderful friend, excellent researcher, great teacher, and true lover of inorganic chemistry and football!

Abstract: The synthesis, crystal structure, and magnetic characterization are reported for three new structurally related iron(III) compounds $(NHEt_3)[Fe_8O_5(OH)_5(O_2PPh_2)_{10}]$ (**1**), $[Fe_{12}\ Ca_4O_{10}(O_2CPh)_{10}(hmp)_4]$ (**2**), and $[Fe_{12}La_4O_{10}(OH)_4(tbb)_{24}]$ (**3**), where hmpH is 2-(hydroxymethyl)pyridine and tbbH is 4-^{t}Bu-benzoic acid. **1** was obtained from the reaction of $Fe(NO_3)_3{\cdot}9H_2O$, diphenylphosphinic acid (Ph_2PO_2H), and NEt_3 in a 1:4:16 molar ratio in MeCN at 50 °C; **2** was obtained from the reaction of $[Fe_3O(O_2CPh)_6(H_2O)_3](NO_3)$, $Ca(NO_3)_2$, and NEt_3 in a 1:1:4:2 ratio at 130 °C; and **3** was obtained from the reaction of $Fe(NO_3)_3{\cdot}9H_2O$, $La(NO_3)_3{\cdot}6H_2O$, 4-^{t}Bu-benzoic acid, and NEt_3 in a 1:1:4:4 ratio in PhCN at 140 °C. The core of **1** consists of two $\{Fe_4(\mu_3\text{-}O)_2\}^{8+}$ butterfly units stacked on top of each other and bridged by O^{2-} and HO^- ions. The cores of **2** and **3** also contain two stacked butterfly units, plus four additional Fe atoms, two at each end, and four M atoms (M = Ca^{2+} (**2**); La^{3+} (**3**)) on the sides. Variable-temperature (T) and solid-state dc and ac magnetization (M) data collected in the 1.8–300 K range revealed that **1** has an S = 0 ground state, **2** has a $\chi_M T$ value at low T consistent with the central Fe_8 in a local S = 0 ground state and the two Fe^{3+} ions in each end-pair to be non-interacting, whereas **3** has a $\chi_M T$ value at low T consistent with these end-pairs each being ferromagnetically coupled with S = 5 ground states, plus intermolecular ferromagnetic interactions. These conclusions were reached from complementing the experimental studies with the calculation of the various Fe_2 pairwise J_{ij} exchange couplings by DFT computations and by using a magnetostructural correlation (MSC) for polynuclear Fe^{3+}/O complexes, as well as a structural analysis of the intermolecular contacts in the crystal packing of **3**.

Keywords: iron-oxo clusters; molecular magnetism; pseudo-carboxylates; exchange interactions; density functional theory; magnetostructural correlation

Citation: Singh, A.P.; Brantley, C.L.; Lee, K.H.K.; Abboud, K.A.; Peralta, J.E.; Christou, G. Structural and Magnetic Analysis of a Family of Structurally Related Iron(III)-Oxo Clusters of Metal Nuclearity Fe_8, $Fe_{12}Ca_4$, and $Fe_{12}La_4$. *Chemistry* **2023**, *5*, 1599–1620. https://doi.org/10.3390/chemistry5030110

Academic Editors: Zoi Lada and Konstantis Konidaris

Received: 1 July 2023
Revised: 18 July 2023
Accepted: 19 July 2023
Published: 24 July 2023

1. Introduction

The chemistry of Fe^{3+}/oxo complexes attracts considerable attention owing to its relevance to a wide range of areas including molecular magnetism [1], bioinorganic chemistry [2], catalysis [3,4], and materials science. Many Fe^{3+}/oxo/carboxylate complexes spanning various nuclearities have been synthesized over the years from Fe_2 [5–11] up to hexameric $[Fe_{28}]_6$ nanocages [12,13]. Dinuclear Fe^{3+} complexes serve as model systems to understand magnetic exchange couplings via magnetostructural correlations (MSCs) and as synthetic analogues of di-iron biomolecules such as ribonucleotide reductase [14–16], methane monooxygenase [14,15,17–20], hemerythrin [21–23], and others [24–26]. Higher nuclearity Fe^{3+}/oxo clusters are highly desired and very useful for studies of interesting magnetic effects such as spin frustration, and even as models of intermediates in the growth

of nanoscale Fe^{3+}/O/OH units within the ferritin Fe storage protein [27–35]. The high charge and Lewis acidity of Fe^{3+} strongly favor the formation of oxide bridges from water molecules and thus higher-nuclearity clusters [27,36,37], and these have been of particular interest within the field of molecular magnetism since spin frustration often leads to a significant ground state spin value [28,38,39] and even single-molecule magnetism. Thus, there is continuing interest in Fe^{3+}/oxo cluster chemistry.

Our work in this area has concentrated on carboxylates, either alone or in conjunction with chelating/bridging groups, and has led to clusters such as, e.g., $[Fe_{18}(pd)_{12}(pdH)_{12}(O_2CPh)_6(NO_3)_6]^{6+}$ (pdH_2 = propane-1,3-diol) [40], which is the largest single-stranded homometallic iron wheel and $[Fe_{22}O_{14}(OH)_3(O_2CMe)_{21}(mda)_6]^{2+}$ (mdaH = *N*-(methyl)diethanolamine) salts. [27] We have also extended our work to various 'pseudo-carboxylates', anionic groups that can bridge metals in a manner analogous to that of carboxylates but with differing electronic and/or steric properties. Their general formula is $[R_xYO_y]^{z-}$, where Y = P, As, S, or Se, x = 1 or 2, y = 2 or 3, and z = 1 or 2, and examples include diphenylphosphinate (Ph_2PO^{2-}), benzenesulfonate ($PhSO^{3-}$), benzeneseleninate ($PhSeO^{2-}$), and dimethylarsinate (Me_2AsO^{2-}) groups. In previous work, we have explored such ligands extensively in Mn/O cluster chemistry [41–47], but related application in Fe/O chemistry has been limited to date [48–52]. Therefore, we have employed diphenylphosphinic acid (Ph_2PO_2H) [53] in the present work.

In addition to the ligand type, we have also explored some reactions that contain a heterometal salt and have chosen diamagnetic La^{3+} and Ca^{2+} for preliminary study for the following reasons: (i) The number of known Fe-lanthanide (Ln) clusters is currently limited and includes $Fe_{12}Ln_4$, $Fe_{14}Gd_{12}$, $Fe_{13}La_6$, $Fe_{22}La_6$, $Fe_{29}M_{16}$, and $Fe_{33}M_{12}$ (M = Y, Gd) [54–58]; and (ii) given our past interest in the Mn_4Ca/oxo cluster that is part of the oxygen-evolving complex (OEC) in the photosynthetic apparatus of green plants and cyanobacteria [59–61], we have found it interesting that the alkaline phosphatase from *P. fluorescens*, PhoX, consists of an Fe_2Ca/oxo cluster with two additional Ca^{2+} ions nearby [62–65]. There are only a few Fe/Ca/oxo clusters in the literature, including moderate nuclearity examples: Fe_2Ca, and two Fe_3Ca clusters with differing oxidation states [64,66,67], and higher-nuclearity $Fe_{14}Ca_{12}$ [68] and Fe_9Ca_2 [69].

A variety of reactions were explored involving different permutations of the above ligand types and metal compositions, as well as metal:ligand and Fe:La(Ca) ratios, reaction temperature, and the additional presence of a chelate such as 2-(hydroxymethyl)pyridine (hmpH). Among the products that could be isolated in pure form and structurally characterized, we noted that three of them are structurally related, in that they all contain the same $\{Fe_8(oxo)_{10}\}$ core unit either alone or as a fragment of a larger core unit, consisting of two butterfly units [28] stacked on top of each other and linked by six additional O^{2-}/HO^- ions. These clusters were $(NHEt_3)[Fe_8O_5(OH)_5(O_2PPh_2)_{10}]$ (**1**), $[Fe_{12}Ca_4O_{10}(O_2CPh)_{10}(hmp)_4]$ (**2**), and $[Fe_{12}La_4O_{10}(OH)_4(tbb)_{24}]$ (**3**), where tbbH is 4-^{t}Bu-benzoic acid. We herein describe the syntheses and structures of **1**–**3**, together with a detailed analysis of their magnetic properties using experimental magnetic susceptibility studies, density functional theory (DFT), and magnetostructural correlation (MSC) methods.

2. Materials and Methods

2.1. Synthesis

All manipulations were performed under aerobic conditions using chemicals as received. $[Fe_3O(O_2CPh)_6(H_2O)_3](NO_3)$ was prepared as described elsewhere [70]. Abbreviations: hmpH = 2-(hydroxymethyl)pyridine; tbbH = 4-^{t}Bu-benzoic acid.

2.1.1. $(NHEt_3)[Fe_8O_5(OH)_5(O_2PPh_2)_{10}]$ (**1**)

To a stirred solution of NEt_3 (1.11 mL, 8.00 mmol) and Ph_2PO_2H (0.436 g, 2.00 mmol) in warm (~50 °C), MeCN (20 mL) was added, $Fe(NO_3)\cdot 9H_2O$ (0.20 g, 0.50 mmol), resulting in an orange suspension. After stirring for 2 h, the reaction was filtered, the resulting orange solid was discarded, and the filtrate was capped and maintained undisturbed at ambient

temperature. After 1 week, the closed cap was replaced with a slow evaporation cap. Well-formed X-ray quality orange crystals of **1**·7MeCN grew over 12 days. These were collected by filtration, washed with Et_2O, and dried under vacuum; the yield was ~9% based on Fe. Selected IR data (KBr pellet, cm^{-1}): 3439(w), 1592(w), 1484(m), 1437(m), 1400(m), 1385(m), 1311(w), 1127(s) 1044(s), 1022(s), 996(s), 925(w), 754(s), 727(s), 693(s), 558(s), 532(s), 471(m), 413(m). Elemental analysis: Calc (Found) for **1**·$\frac{1}{2}$MeCN ($C_{127}H_{122\cdot5}N_{1\cdot5}Fe_8P_{10}O_{30}$): C 52.49 (51.95), H 4.25 (4.32), N 0.72 (0.85)%.

2.1.2. $[Fe_{12}Ca_4O_{10}(O_2CPh)_{20}(hmp)_4]$ (**2**)

To a stirred solution of $Ca(NO_3)_2{\cdot}4H_2O$ (0.030 g, 0.125 mmol), hmpH (0.055 g, 0.50 mmol) and NEt_3 (0.350 mL, 0.25 mmol) in MeCN/MeOH (11 mL; 10:1 v/v) was added as a solid $[Fe_3O(O_2CPh)_6(H_2O)_3](NO_3)$ (0.13 g, 0.125 mmol), resulting in a brown slurry. The mixture was heated in a microwave reactor for 20 min at 130 °C, and the resulting dark red solution was filtered, and the filtrate was left undisturbed at ambient temperature. After 3–5 days, X-ray quality red block crystals of **2**·(solv) had formed. These were collected by filtration, washed with MeCN and Et_2O, and dried under vacuum; the yield was ~10% based on Fe. Selected IR data (KBr, cm^{-1}): 3422(br), 2934(w), 1601(s), 1545(s), 1405(vs), 1069(m), 1047(m), 764(w), 718(s), 678(m), 578(w), 464(m). Elemental analysis: Calc (Found) for **2**·$2H_2O$ ($C_{164}H_{128}N_4Ca_4Fe_{12}O_{56}$): C 50.75 (50.47), H 3.32 (3.37), N 1.44 (1.49)%.

2.1.3. $[Fe_{12}La_4O_{10}(OH)_4(tbb)_{24}]$ (**3**)

Method A. To a stirred colourless solution of (tbbH) (0.71 g, 4.0 mmol) in benzonitrile (PhCN) (10 mL) in a microwave reaction vial was added NEt_3 (0.56 mL, 4.0 mmol) followed by $Fe(NO_3)_3{\cdot}9H_2O$ (0.40, 1.0 mmol) and $La(NO_3)_3{\cdot}6H_2O$ (0.43, 1.0 mmol) was added, resulting in a brown solution. This was stirred for a further 5 min at room temperature and then the vial was sealed and heated at 140 °C in a microwave reactor for 1 h. After cooling to room temperature, the vial was removed from the microwave reactor, and the obtained near-black solution was mixed with CH_2Cl_2 (5 mL) and then filtered to remove any undissolved solids. The filtrate was layered with MeCN and left undisturbed in a sealed vial at ambient temperature for 3 days, during which time orange-red crystals of **3**·5PhCN had formed. These were collected by filtration, washed with Me_2CO, and dried under vacuum; the yield was ~15% based on Fe. Selected IR data (KBr, cm^{-1}): 3422(br), 2362(m), 2336(m), 1611(w), 1592(m), 1534(m), 1412(br), 784(m), 711(m), 590(m), 543(m), 468(m), 427(m). Elemental analysis: Calc. (Found) for **3**·5PhCN·$2H_2O$ ($C_{299}H_{345}N_5Fe_{12}La_4O_{64}$): C, 57.38 (57.13); H, 5.56 (5.37); N, 1.12 (0.91)%.

Method B. The above procedure was repeated in MeCN (15 mL) as a solvent instead of PhCN. After cooling the microwave reaction vial to ambient temperature, a yellow-orange precipitate was collected by filtration and washed with MeCN. It was dissolved in CH_2Cl_2 (10 mL) and layered with an equal volume of EtOH. After two days, X-ray quality orange-red crystals had grown, and these were collected by filtration, washed with Me_2CO, and dried under vacuum. The product was confirmed to be **3** by infrared spectral comparison with the product from Method A. The yield was ~45% based on Fe. Elemental analysis: Calc. (Found) for **3**·$4H_2O$ ($C_{264}H_{324}O_{66}Fe_{12}La_4$): C, 54.87 (54.95); H, 5.65 (5.73); N, 0.00 (0.0)%.

2.2. X-ray Crystallography

Single-crystal X-ray data were collected at 100 K on a Bruker Dual micro source D8 Venture diffractometer and PHOTON III detector running APEX4 software package of programs and using MoK_α radiation (λ = 0.71073 Å). The data frames were integrated, multi-scan scaling was applied, and the intrinsic phasing structure solution provided all the non-H atoms. The structures were refined using full-matrix least-squares cycles [71]. Non-H atoms were refined with anisotropic displacement parameters, and all H atoms were placed in calculated, idealized positions and refined riding on their parent atoms. The refinements were carried out on F^2 by minimizing the wR_2 function; R_1 is calculated

to provide a reference to the conventional *R* value but its function was not minimized (Table 1).

Table 1. Crystal data and structural refinement parameters for **1**–**3**.

	1	**2**	**3**
Formula [a]	$C_{126}H_{115}Fe_8NO_{30\cdot50}P_{10}$	$C_{163\cdot6}H_{122\cdot4}Fe_{12}Ca_4N_{3\cdot6}O_{55\cdot6}$	$C_{161\cdot76}H_{177\cdot25}Fe_6La_2N_{4\cdot25}O_{31}$
Fw, g/mol	2887.68	3858.76	3289.74
Crystal system	Orthorhombic	Monoclinic	Triclinic
Space group	*P*bca	$P2_1/c$	$P\bar{1}$
a, Å	25.7321(8)	18.4877(16)	19.6897(9)
b, Å	29.8328(9)	23.1092(19)	21.5274(10)
c, Å	37.9740(12)	23.7055(19)	24.0099(11)
α, °	90	90	97.3530(10)
β, °	90	112.917(2)	111.5360(10)
γ, °	90	90	115.5490(10)
Volume, Å^3	29,151.1(16)	9328.4(13)	8028.5(6)
Z	8	2	2
T, K	100(2)	100(2)	100(2)
λ, Å [a]	0.71073	0.71073	0.71073
$\rho_{calc,}$ Mg/m^3	1.316	1.374	1.361
R_1 [b, d]	4.49	5.89	4.72
wR_2 [c, e]	9.90	15.00	11.52

[a] solvent molecules not included. [b] Graphite monochromator. [c] $I > 2\sigma(I)$. [d] $R_1 = \Sigma(||F_o| - |F_c||)/\Sigma|F_o|$. [e] $wR_2 = [\Sigma[w(F_o^2 - F_c^2)^2]/\Sigma[w(F_o^2)^2]]^{1/2}$ where $w = 1/[\sigma^2(F_o^2) + (m \times p)^2 + n \times p]$, $p = [\max(F_o^2,0) + 2 \times F_c^2]/3$, and *m* & *n* are constants.

For **1**·7MeCN, the asymmetric unit consists of a complete Fe_8 cluster anion, one $NHEt_3^+$ cation, and seven MeCN solvent molecules disordered over 9 positions. The cluster has one disordered phenyl ring and was refined in two parts; partial H_2O solvent molecules accompany the disorder. The solvent molecules were too disordered to be properly refined, and thus the program SQUEEZE/PLATON [72,73] was applied to remove the solvent contribution to the total diffraction intensity of 5728 Å^3 and 1312 electrons per cell. Five hydroxyl protons were obtained from a Difference Fourier map and refined freely, H5, H6, H7, H8 and H111. In the final cycle of refinement, 50,378 reflections (of which 35,688 are observed with $I > 2\sigma(I)$) were used to refine 1646 parameters, and the resulting R_1, wR_2, and *S* (goodness of fit) were 4.49%, 9.90%, and 1.015, respectively.

For **2**·(solv), the asymmetric unit consists of a half $Fe_{12}Ca_4$ cluster located on an inversion center and a mixture of disordered MeCN and MeOH solvent molecules accounting for the removal of 254 electrons per cell and a total void of 1256 Å^3. The cluster exhibits a disorder over three iron centers where part one has two coordinated two 2-hydroxymethylpyridine and benzoate ligands and partial methanol and acetonitrile solvent molecules. In the final cycle of refinement, 21,402 reflections (of which 17,520 are observed with $I > 2\sigma(I)$) were used to refine 868 parameters, and the resulting R_1, wR_2, and *S* (goodness of fit) were 5.89%, 15.00%, and 1.107, respectively.

For **3**·5PhCN, the asymmetric unit consists of a half $Fe_{12}La_4$ cluster lying on an inversion center and three PhCN molecules. Most of the cluster ligands and two of the PhCN molecules are disordered to various degrees, and each was refined in two positions. The third PhCN was present at only 50% occupancy, giving a total of 5 PhCN per cluster. In the final cycle of refinement, 28,232 reflections (of which 23,130 are observed with $I > 2\sigma(I)$) were used to refine 1825 parameters and the resulting R_1, wR_2, and *S* (goodness of fit) were 4.72%, 11.52%, and 1.090, respectively.

2.3. Physical Measurements

Infrared spectra in the 400–4000 cm^{-1} range were recorded in the solid state (KBr pellets) using a Nicolet iS5 FTIR spectrometer. Elemental analyses (C, H, and N) were performed by Atlantic Microlabs in Norcross, GA, USA. Metal oxidation states were determined from bond valence sum (BVS) calculations [74,75]. Variable temperature dc and ac magnetic susceptibility data were collected on vacuum-dried samples using a Quantum Design MPMS-XL superconducting quantum interference device (SQUID) magnetometer, capable of operating with applied dc fields up to 7 T. Microcrystalline samples were restrained in solid eicosane to prevent torquing. Dc magnetic susceptibility data were collected under a constant 0.1 T applied field in the 5.0–300 K temperature range. Ac magnetic susceptibility studies were performed using a 3.5 G applied ac field in frequencies up to 1000 Hz and in the 1.8–15 K range. Pascal's constants were used to estimate the diamagnetic correction, and eicosane and gel capsule contributions were measured as a blank. These values were subtracted from the experimental susceptibility to provide the molar paramagnetic susceptibility (χ_M) [76].

2.4. Theoretical Calculations

DFT calculations on $Fe_{12}La_4$ complex **3** were performed using the crystal structure coordinates. A total of 24 distinct J_{ij} nearest-neighbour exchange couplings were determined from DFT calculations by mapping broken-symmetry solutions to Ising-type spin configurations, $\{S\}$. The employed configurations were one high spin (all spins parallel), all 12 possible single-spin inversions, and all 24 nearest-neighbor two-spin inversions, giving a total of 37 broken-symmetry solutions. The energies of these configurations are expressed in terms of a sum over spin interactions (Equation (1)), where $\langle ij \rangle$ stands for all neighbouring ij pairs, $S_k = \pm^5/_2$ for Fe^{3+}, and E_0 is a constant introduced to match the spin model with the DFT energies.

$$E(\{S\}) = E_0 - 2\sum_{\langle ij \rangle} J_{ij} S_i \cdot S_j \quad (1)$$

The energies of all configurations $\{S\}$ resulting from the broken spin-symmetry DFT calculations were used as the l.h.s. of Equation (1) to perform a linear fit and determine all the exchange couplings, J_{ij}. This same approach has been successfully used in the literature to determine exchange couplings in multicenter transition metal complexes [77–81]. In our case, the R^2 coefficient of the linear regression differs from 1 by less than 10^{-6}, indicating that the magnetization is well localized at the magnetic centers, thus the broken spin-symmetry DFT solutions are reliable representations of the Ising-type model spin configurations. For all cases, the atomic spin populations of the DFT calculations are consistent with the expected broken spin-symmetry configurations.

In all DFT calculations, the hybrid Perdew–Burke–Ernzerhof (PBEh) density functional approximation, an admixture of exactly 25% (Hartree-Fock-type) exchange and 75% PBE exchange, is known to perform well for magnetic exchange couplings [82], and thus was employed. An RMS error of approximately 10%, was determined for the particular case of oxo-bridged Fe_2 couplings, as shown for a set of eleven dinuclear Fe^{3+} complexes [83]. Pople's all-electron 6-311+G** basis was used for Fe atoms, 6-31G** for lighter elements [84–86], and the segmented all-electron relativistically contracted SARC-DKH2 basis for La atoms [87]. In all calculations, scalar relativistic effects were included through the second-order Douglass–Kroll–Hess approximation [88–90]. An in-house version of the Gaussian 16 program [91] was used for all broken-symmetry DFT energies obtained, which allowed for spin inversions of the individual magnetic centers to produce a suitable initial guess for self-consistent broken spin-symmetry calculations. No point group symmetry was assumed at any point in the model or the DFT calculations. Self-consistency convergence thresholds of 10^{-6} Ha = 0.2 cm^{-1} in the energy and 10^{-8} in the RMS changes in the density matrix were used in all calculations.

3. Results

3.1. Synthesis

As stated in the introduction, many reactions were explored involving different permutations of metal sources, ligands, and other reaction parameters. Complexes **1**–**3** were obtained from overall similar reaction systems that nevertheless had some distinct differences: the Fe^{III} source was either $Fe(NO_3)_3$ or the preformed trinuclear $[Fe_3O(O_2CPh)_6(H_2O)_3]^+$ cluster; the peripheral ligands were either carboxylates or pseudo-carboxylate $Ph_2PO_2^-$ groups; the reactions were homo- or heterometallic; the chelate hmpH was either included or not; the solvents were MeCN, MeCN/MeOH, or PhCN; and the reactions were carried out in the 50–140 °C range under thermal or microwave heating. The overall unifying theme is that **1**–**3** all contain the same central Fe_8 unit. The yields were generally low (~10%), but through crystallographic identification of **3** we were able to then devise a rational synthesis that greatly increased the yield to ~45%.

3.2. Description of Structures

Complex **1** crystallizes in the orthorhombic space group *P*bca with the asymmetric unit containing the complete Fe_8 anion. The structure of the latter and its labeled core are shown in Figure 1; a stereopair is provided in Figure S1 (Supplementary Materials). The core consists of two $\{Fe_4(\mu_3\text{-}O)_2\}^{8+}$ butterfly units, common structural units in Fe_4 cluster chemistry [28,92–100], stacked on top of each other and bridged by one O^{2-} and five HO^- ions. The octahedral Fe^{III} oxidation states (Table S1, Supplementary Materials) and the protonation level of core O atoms (Table 2) were confirmed by Fe and O bond valence sum (BVS) calculations, respectively [74,75]; BVS values for all core and ligand O atoms are listed in Table S2. The BVS of O^{2-} ion O112 is 1.55, lower than expected because it is involved in a hydrogen-bond with the $NHEt_3^+$ cation (O112···H-N = 2.807(3)Å), akin to a 'partial-protonation'. Peripheral ligation about the $\{Fe_8O_5(OH)_5\}^{9+}$ core is provided by ten $\eta^1{:}\eta^1{:}\mu_2\text{-}PhPO_2^-$ groups, and the complete cation has virtual D_{2h} symmetry, ignoring the disorder and rotation positions of the Ph rings.

Table 2. BVS values and assignments for core O atoms of the anion of **1** and **3**.

Complex	Atom	BVS	Assignment [a]
1	O1	1.86	O^{2-}
	O2	1.86	O^{2-}
	O3	1.87	O^{2-}
	O4	1.91	O^{2-}
	O5	0.98	OH^-
	O6	1.00	OH^-
	O7	1.02	OH^-
	O8	0.81	OH^-
	O111	1.24	OH^-
	O112	1.55 [b]	O^{2-} [b]
3	O1	1.72	O^{2-}
	O2	1.73	O^{2-}
	O3	1.83	O^{2-}
	O4	2.07	O^{2-}
	O5	1.14	OH^-
	O6	2.01	O^{2-}
	O7	1.15	OH^-

[a] Non-, singly, and doubly protonated O atoms have typical BVS values of ~1.8 to 2.0, ~0.9 to 1.2, and ~0.2 to 0.4, although H-bonding can affect the ranges. [b] Decreased from a typical O^{2-} value due to hydrogen-bonding with the $NHEt_3^+$ cation.

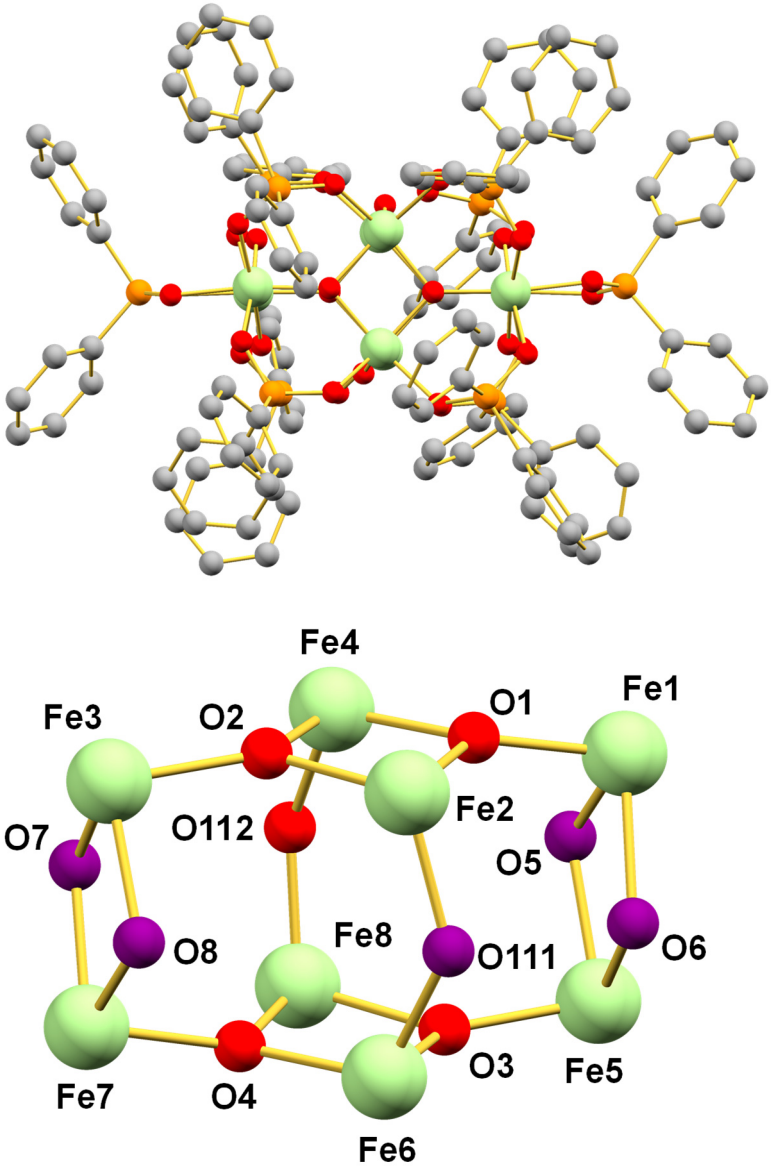

Figure 1. (**top**) Complete structure of the anion of **1** from a viewpoint parallel to the stacking axis of the two Fe_4 butterfly units. H atoms are omitted for clarity. (**bottom**) Labeled $\{Fe_8O_5(OH)_5\}^{8+}$ core from a viewpoint nearly perpendicular to the stacking axis. Colour code: Fe^{3+} light green, P orange, O red, HO^- purple, C grey.

Complex **2** crystallizes in the monoclinic space group $P2_1/c$ with the asymmetric unit containing half the $Fe_{12}Ca_4$ cluster. The structure (without aromatic rings for clarity) from two viewpoints and the partially labeled core are shown in Figure 2; a stereopair of the complete molecule is provided in Figure S2. Additionally, **2** contains the same core of two stacked butterfly units as seen in the anion of **1**, but now all its inter-butterfly bridging ions are O^{2-} (i.e., $\{Fe_8O_{10}\}^{4+}$) because they are attached to additional metal ions: (i) on each end is an attached $\{Fe_2(\mu_3\text{-}OR)_2\}$ unit forming an $\{Fe_4O_2(\mu_3\text{-}OR)_2\}$ cubane, where RO^- is the alkoxide arm of an hmp^- N,O chelate; and (ii) on each side two seven-coordinate pentagonal bipyramidal Ca^{2+} ions are attached, each of them connecting to a cubane μ_3-O^{2-} ion, making them μ_4, and to one of the central μ_2-O^{2-} ions bridging two butterfly units, making it a μ_4-O^{2-} that bridges two Ca^{2+} ions. Fe and O BVS calculations were again used to confirm Fe^{III} oxidation states and non-protonated core O^{2-} ions (Table S3). Peripheral ligation is by 4 η^1:η^3:μ_4-hmp^-, 12 η^1:η^1:μ_2-$PhCO_2^-$, and 8 η^1:η^2:μ_3-$PhCO_2^-$ groups, the latter providing further linkages between the central $\{Fe_8O_{10}\}^{4+}$ unit and the

Ca^{2+} ions. Four of the $\eta^1{:}\eta^2{:}\mu_3$-$PhCO_2^-$ groups bridge FeCa pairs, two bridge the butterfly 'body' Fe_2 pairs, and two bridge Ca_2 pairs.

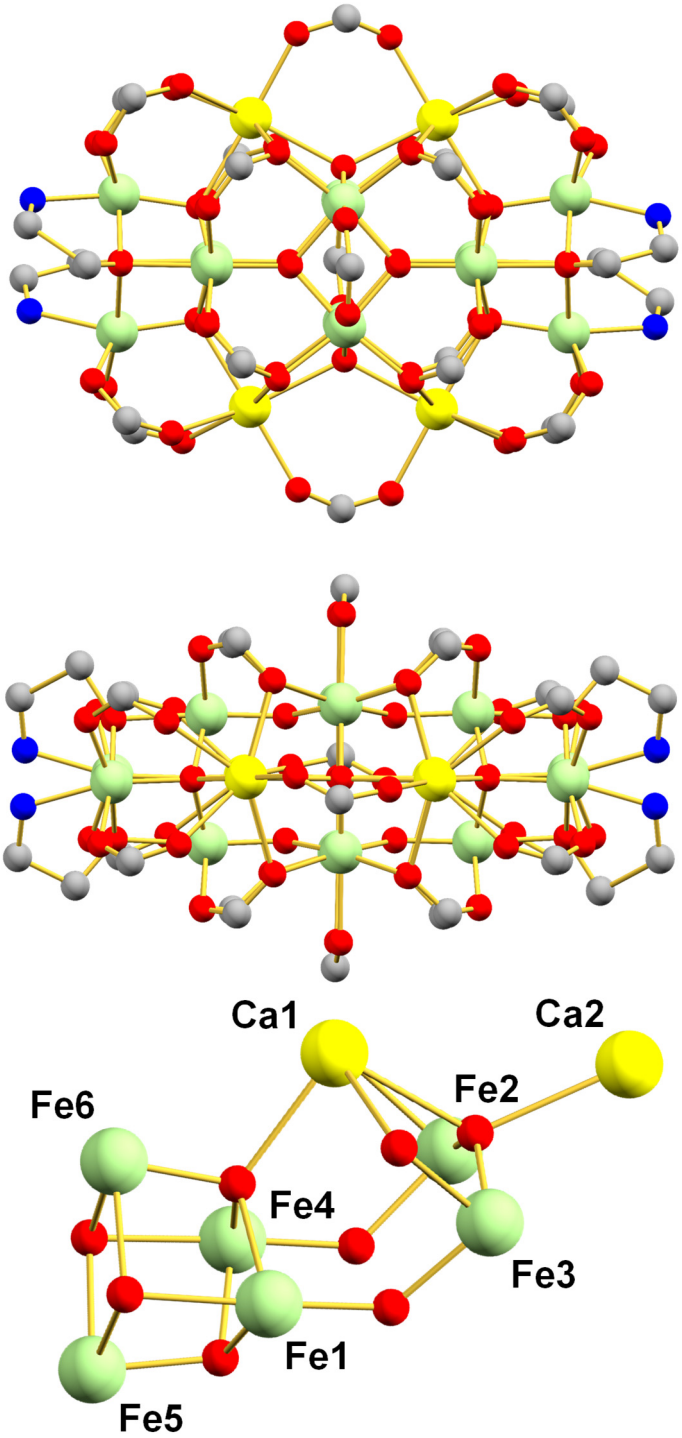

Figure 2. Partial structure of **2** from viewpoints parallel (**top**) and perpendicular (**middle**) to the stacking axis. H atoms and aromatic rings are omitted for clarity. **(bottom)** Partially labeled half of the core emphasizing the means of attachment of the end Fe_2 unit and Ca^{2+} ions. Color code: Fe^{3+} light green, Ca^{2+} yellow, O red, N blue, and C grey.

Complex **3** crystallizes in the triclinic space group $P\bar{1}$ with the asymmetric unit containing half the $Fe_{12}La_4$ cluster. The structure (without 4-^{t}Bu-Ph groups for clarity) from two viewpoints and the partially labeled core is shown in Figure 3; a stereopair of the

complete molecule is provided in Figure S2. Furthermore, **3** contains the same core of two stacked butterfly units as seen in **2** and the anion of **1**, and its overall structure is similar to that of **2** except for the following: (i) four nine-coordinate tricapped trigonal prismatic La^{3+} ions have replaced the four Ca^{2+}; and (ii) the cubanes at each end are now $\{Fe_4O_2(\mu_3\text{-}OH)_2\}$ with an $\eta^1{:}\eta^1{:}\mu_2\text{-}RCO_2^-$, instead of the two chelating/bridging hmp^- groups. Fe^{III} oxidation states and protonation levels of core O^{2-}/HO^- ions were again confirmed by BVS calculations (Table 2 and Table S4). Peripheral ligation is by 14 $\eta^1{:}\eta^1{:}\mu_2\text{-}{}^t\text{BuPhO}_2^-$, 8 $\eta^1{:}\eta^2{:}\mu_3\text{-}{}^t\text{BuPhO}_2^-$, and 2 $\eta^1{:}\eta^2{:}\mu_2\text{-}{}^t\text{BuPhO}_2^-$ groups, which are disposed as for **2,** except that owing to the higher coordination number of La^{3+} vs. Ca^{2+}, the La_2 pairs on each side are now each bridged by two carboxylates, one $\eta^1{:}\eta^1{:}\mu_2\text{-}{}^t\text{BuPhO}_2^-$ and the other $\eta^1{:}\eta^2{:}\mu_3\text{-}{}^t\text{BuPhO}_2^-$.

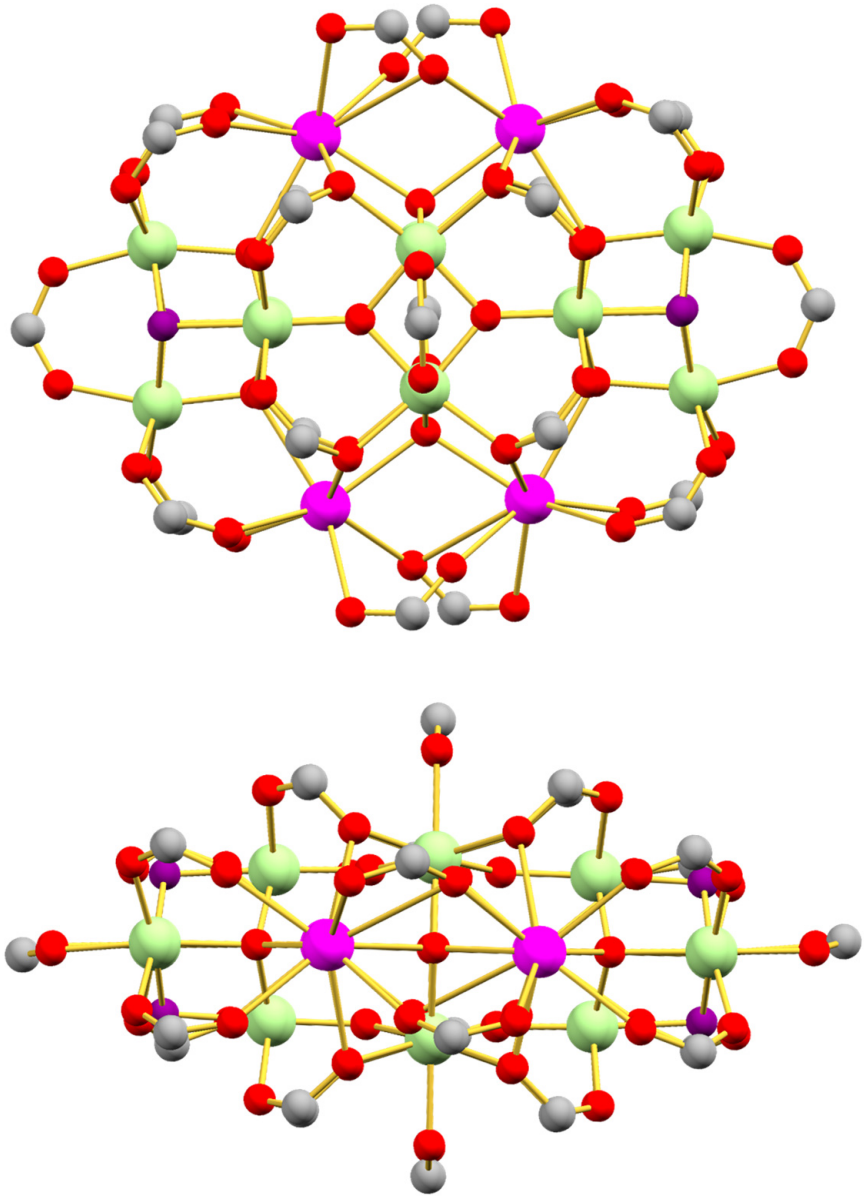

Figure 3. *Cont.*

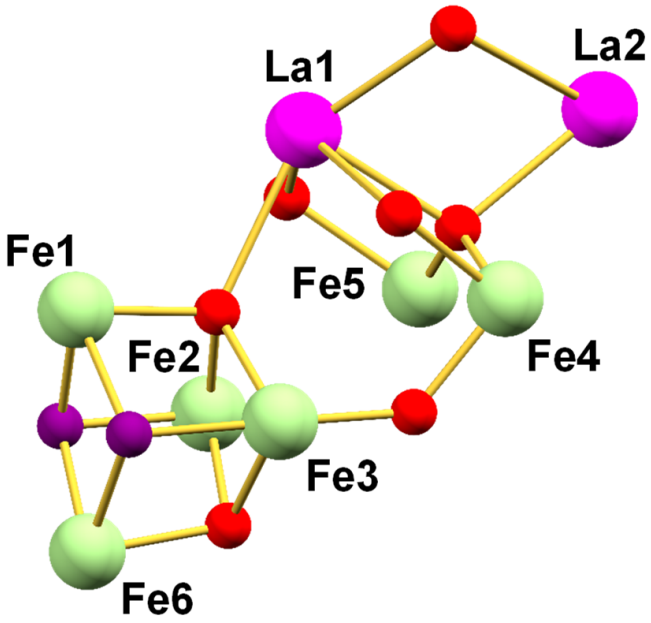

Figure 3. Partial structure of **3** from viewpoints parallel (**top**) and perpendicular (**middle**) to the stacking axis. H atoms and aromatic rings are omitted for clarity. (**bottom**) Partially labeled half of the core emphasizing the means of attachment of the end Fe_2 unit and La^{3+} ions. Color code: Fe^{3+} light green, La^{3+} magenta, O red, HO^{-} purple, and C grey.

The degree of similarity between the Fe_8 core of **1** and those within the cores of **2** and **3** was assessed by carrying out root-mean-square-difference (RMSD) calculations for the cores of **1** vs. **2** and **1** vs. **3**. The results are listed in Tables S5 and S6, respectively, and shown pictorially in Figure 4. The RMSD values are only 0.096 and 0.109 Å, respectively, and the overall conclusion is therefore that the Fe_8 units within the three compounds are essentially superimposable.

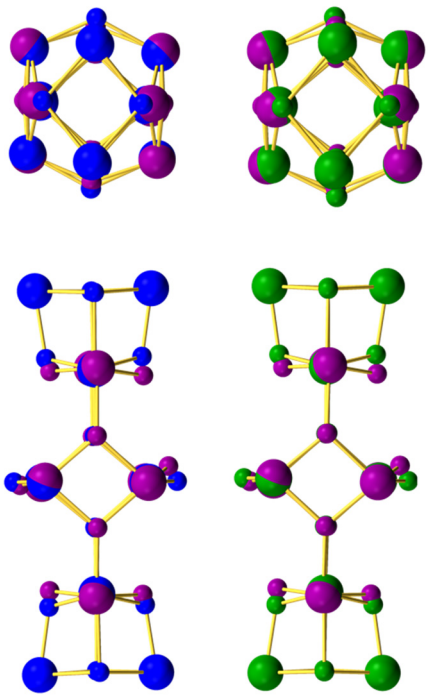

Figure 4. RMSD overlay of the core of the anion of **1** on the cores of **2** (**left**) and **3** (**right**) from two perpendicular viewpoints each. Color code: **1** purple, **2** blue, **3** green.

3.3. SQUID Magnetometry

3.3.1. Dc Magnetic Susceptibility Studies

Solid-state, variable-temperature dc magnetic susceptibility (χ_M) data were collected on vacuum-dried microcrystalline samples of **1**·$\frac{1}{2}$MeCN, **2**·2H_2O and **3**·4H_2O, restrained in eicosane to prevent torquing, in a 1.0 kG (0.10 T) magnetic field and a 5.0 to 300 K temperature range. The data are plotted as $\chi_M T$ vs. T in Figure 5.

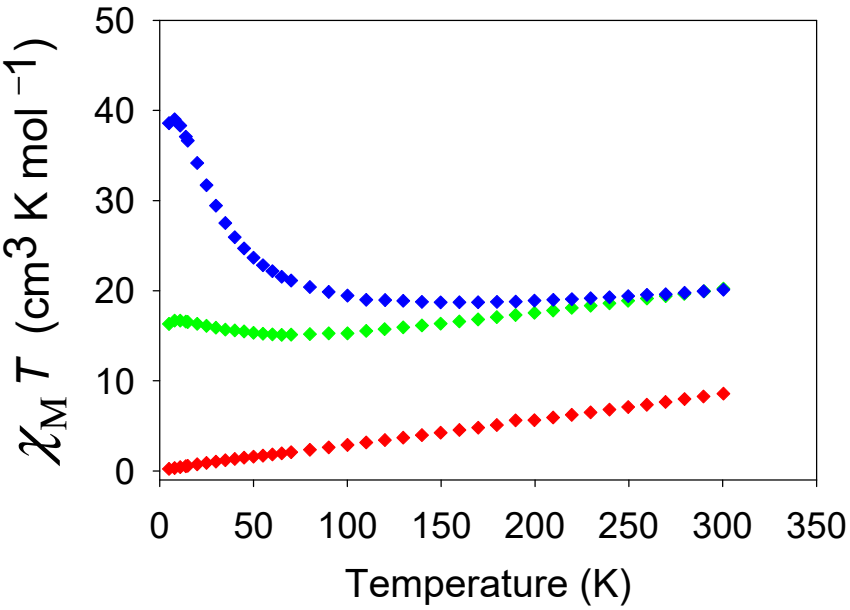

Figure 5. Plots of dc $\chi_M T$ vs. T in the 5.0–300 K range and a 0.1 T dc field for vacuum-dried **1**·$\frac{1}{2}$MeCN (♦), **2**·2H_2O (♦), and **3**·4H_2O (♦).

For **1**·$\frac{1}{2}$MeCN, $\chi_M T$ decreases monotonically and near-linearly from 8.57 cm^3 K mol^{-1} at 300 K to 0.22 cm^3 K mol^{-1} at 5.0 K. The 300 K value is much lower than the spin-only (g = 2.0) value of 35.0 cm^3 K mol^{-1} for eight non-interacting Fe^{3+} ions ($S = {}^5/_2$) indicates strong antiferromagnetic (**AF**) interactions within the cluster, and the 5.0 K value and plot profile indicate an S = 0 ground state.

For **2**·2H_2O, $\chi_M T$ decreases from 20.23 cm^3 K mol^{-1} at 300 K to a minimum of 15.09 cm^3 K mol^{-1} at 65 K and then increases to a maximum of 16.68 cm^3 K mol^{-1} at 8.0 K before a final slight decrease to 16.31 cm^3 K mol^{-1} at 5.0 K (Figure 5). The 300 K value is again much smaller than the spin-only value for twelve non-interacting Fe^{3+} ions of 52.50 cm^3 K mol^{-1} indicating strong **AF** interactions. Given the structural similarity between the three clusters, it is reasonable to propose that **2** consists of a strongly **AF** central Fe_8 unit with an S = 0 local ground state, as seen for the anion of **1**, and a Fe_2 pair at each end that is responsible for the observed $\chi_M T$ at the lowest temperatures. Entertaining this possibility further, the 16.68 cm^3 K mol^{-1} at 8.0 K would be consistent with four non-interacting Fe^{3+} ions (spin-only $\chi_M T$ = 17.5 cm^3 K mol^{-1}), suggesting little or no interaction within each Fe_2 pair. This possibility will be assessed further below (vide infra).

For **3**·4H_2O, $\chi_M T$ decreases from 20.11 cm^3 K mol^{-1} at 300 K to a minimum of 18.71 cm^3 K mol^{-1} at 150 K and then increases to a maximum of 39.01 cm^3 K mol^{-1} at 8.0 K before a final drop to 38.59 cm^3 K mol^{-1} at 5.0 K (Figure 5). The 300 K value is similar to that for **2**·2H_2O, and indeed the $\chi_M T$ vs. T profiles of the two complexes are somewhat similar except that $\chi_M T$ for **3**·4H_2O increases to much higher values at the lowest T. Based on the proposed explanation for the $\chi_M T$ vs. T profile for **2**·2H_2O, we suggest that the coupling within the Fe_2 pairs at each end is now ferromagnetic (**F**), leading to each Fe_2 having an S = 5 ground state. However, the spin-only $\chi_M T$ for two independent S = 5 units is 30.0 cm^3 K mol^{-1}, significantly below the 8.0 K value. The latter is more consistent with

two $S = 6$ units (spin-only $\chi_M T = 42.0$ cm^3 K mol^{-1}) but this seemed very unlikely, and it was clear that additional studies were necessary to resolve this problem (vide infra).

3.3.2. Ac Magnetic Susceptibility Studies

To remove the possibility of any complicating effect of the dc field on the lowest T data, especially when studying complexes with some very weak couplings, alternating current (ac) magnetic susceptibility studies were carried out in the 1.8–15.0 K range using a 3.5 G ac field at a 1000 Hz oscillation frequency, and with no applied dc field. The obtained ac in-phase (χ'_M) susceptibility of the three complexes is plotted as $\chi'_M T$ vs. T in Figure 6. For **1**·$\frac{1}{2}$MeCN, $\chi'_M T$ is essentially zero below 15.0 K, confirming a well-isolated $S = 0$ ground state spin as deduced from the dc data. For **2**·H_2O, $\chi'_M T$ is essentially constant below 15.0 K at ~17.0 cm^3 K mol^{-1}, in agreement with the dc data suggesting four non-interacting Fe^{3+} ions. For **3**·$4H_2O$, we were very interested to see that $\chi'_M T$ agreed with the dc $\chi_M T$ data, with a plateau value at 6–10 K of ~40.5 cm^3 K mol^{-1}, confirming that the surprisingly high value is not an artifact of the dc field.

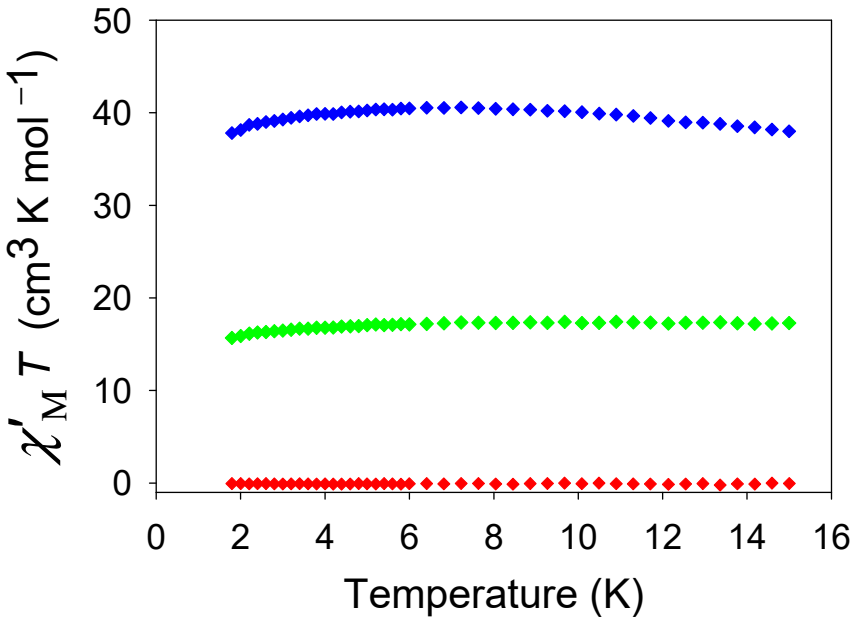

Figure 6. Plots of ac in-phase $\chi'_M T$ vs. T in the 1.8–15.0 K range and a 0.35 G ac field at a 1000 Hz frequency for vacuum-dried **1**·$\frac{1}{2}$MeCN (♦), **2**·$2H_2O$ (♦), and **3**·$4H_2O$ (♦).

3.3.3. Ground State Spin Rationalization Using a Magnetostructural Correlation (MSC)

Generally, a fit of magnetic susceptibility data is used to assess coupling constants between magnetic ions in cluster chemistry; however, high nuclearity clusters are difficult to simulate and the experimental data is difficult to fit. Therefore, a more quantitative rationalization of the magnetic data requires attainment of the constituent pairwise Fe_2 exchange interactions, J_{ij}, within the three clusters. However, given their high nuclearity, low symmetry, and many symmetry-inequivalent J_{ij} even for the anion of **1**, we could not obtain them from fits of experimental data. We thus employed the magnetostructural correlation (MSC) that we developed specifically for high nuclearity Fe^{III}/oxo clusters, which yields estimates of the J_{ij} couplings from Fe-O-Fe angles (ϕ) and average Fe-O bond lengths (r) for each Fe_2 pair [101]. The MSC (Equation (2)) is based on the angular overlap model and the $H = -2J_{ij}\hat{S}_i \cdot \hat{S}_j$ convention.

$$J = (1.23 \times 109)(-0.12 + 1.57\cos\phi + \cos 2\phi)\exp(-8.99r) \quad (2)$$

The Fe-O and Fe-O-Fe values for each Fe_2 pair were used to generate the J_{MSC} values for **1**–**3**, and these are listed in Table 3. For comparison, we also carried out DFT calcula-

tions on representative **3** using the broken-symmetry approach, and the resulting J_{DFT} are provided in Table 3. Because of the very similar Fe_8 units in **1**–**3**, we did not carry out DFT calculations on **1** and **2**.

Table 3. Exchange interactions J_{ij} for Fe_2 pairs in **1**–**3**.

Pair	J_{MSC} 1 [a]	Pair	J_{MSC} 2 [a]	Pair	J_{MSC} 3 [a]	J_{DFT} 3 [a]
Fe1–Fe2	−26.9	Fe1–Fe2	−33.5	Fe2–Fe4	−52.4	−44.9
Fe1–Fe4	−20.9	Fe1–Fe3	−32.3	Fe2–Fe5	−53.0	−44.3
Fe2–Fe3	−26.2	Fe2–Fe4	−28.1	Fe3–Fe4	−54.3	−46.3
Fe3–Fe4	−25.4	Fe3–Fe4	−29.3	Fe3–Fe5	−53.7	−44.2
Fe2–Fe4	−8.8 [b]	Fe2–Fe3	−7.6 [b]	Fe4–Fe5	−14.8	+0.8 [b]
Fe5–Fe6	−29.4	Fe1–Fe4	−3.2	Fe4–Fe5′	−27.4	−27.4
Fe5–Fe8	−20.5	Fe1–Fe5	−0.9	Fe1–Fe6	−3.7	−0.1 [d]
Fe6–Fe7	−25.7	Fe1–Fe6	−1.5	Fe3–Fe6	−9.6	−7.5
Fe7–Fe8	−29.4	Fe2–Fe3′	−36.3	Fe2–Fe6	−10.2	−7.8
Fe6–Fe8	−9.9 [b]	Fe4–Fe5	−1.3	Fe2–Fe3	−2.3	+2.0
Fe1–Fe5	−5.4	Fe4–Fe6	−0.8	Fe1–Fe2	−10.1	−8.0
Fe3–Fe7	−2.3	Fe5–Fe6	−1.9 [d]	Fe1–Fe3	−8.6	−5.1
Fe2–Fe6	−24.7					
Fe4–Fe8	−51.7 [c]					

[a] cm^{-1}. [b] Body-body pairs within the Fe_4 butterfly units. [c] This is the Fe4-O112-F8 unit, the only Fe_2 pair with a μ_2-O^{2-} bridge, rationalizing a much stronger J_{MSC} even though O112 is involved in hydrogen-bonding with the $NHEt_3^+$ cation. [d] Fe_2 pairs attached to each end of the central Fe_8 unit giving the cubanes.

Elucidating the magnetic properties of the Fe_8 anion of **1** is also important in allowing interpretation of the magnetic properties of the larger Fe_{12} cores of **2** and **3** that contain an Fe_8 sub-unit. The J_{MSC} for the anion of **1** separates into three groups: weak, strong, and very strong. Within each Fe_4 butterfly, the body-body (J_{bb}) interactions (Fe2Fe4 and Fe6Fe8) are weak (−8.8 and −9.9 cm^{-1}, respectively), as expected for bis-monoatomically bridged Fe_2 pairs with their smaller Fe-O-Fe angles (<100°) [13,39,51,102]. In contrast, the wingtip-body (J_{wb}) interactions within each butterfly are strong (−20.9 to −29.4 cm^{-1}), reflecting their single monoatomic bridge and consequently larger angles (127–132°). Since each butterfly unit comprises two edge-fused Fe_3 triangles and all the intra-butterfly interactions are **AF**, there will be spin frustration effects operating (competing exchange interactions). However, within each Fe_3 triangle, the one weak J_{bb} is competing with two strong J_{wb} so the former is completely frustrated and the J_{wb} are satisfied, i.e., the spin vector alignments are determined only by the J_{wb} (Figure 7). There are four inter-butterfly interactions, two of which (Fe1Fe5 and Fe3Fe7) are again weak (−5.4 and −2.3 cm^{-1}, respectively) due to being bis-monoatomically bridged. The third is Fe2(μ_2-OH)Fe6 and is strong (−24.7 cm^{-1}), whereas the fourth is Fe4(μ_2-O)Fe8 and is very strong (−51.7 cm^{-1}), the difference assignable to the latter's shorter Fe-O bonds (av. 1.855 Å) compared with the former's Fe-OH bonds (av. 1.936 Å) since the Fe-O-Fe angles are similar (138.63 vs. 134.75°, respectively). The inter-butterfly interactions are not competing with each other nor the intra-butterfly ones, and they are therefore all satisfied, even the weakest ones. This provides the overall spin vector alignments shown in Figure 7, rationalizing the experimentally observed $S = 0$ ground state.

The J_{MSC} of the central Fe_8 subunit of **2** shows that the J_{bb} (Fe2Fe3) are again weak (−7.5 cm^{-1}) and the J_{wb} are again strong (−28.1 to −33.5 cm^{-1}), slightly stronger than those for **1**. The latter is assigned to the extra Fe^{3+} and Ca^{2+} ions affecting the Fe-O bond lengths in **2**; for example, the average wingtip Fe-μ_3-O^{2-} lengths decrease from 1.924 Å in **1** to 1.853 Å in **2**, giving stronger J_{wb} in **2**. The central Fe_8 of **2** should thus have an $S = 0$ local ground state (Figure 8), analogous to **1**, and the overall ground state is thus determined by the intra-Fe_2 coupling within the Fe_2 pairs at each end. If each intra-Fe_2 coupling were **AF**, as shown arbitrarily in Figure 8, then **2** would have an overall $S = 0$ ground state, which it clearly does not; both the dc and ac data indicate four essentially non-interacting Fe^{3+} ions. In fact, this is consistent with the very weak J_{MSC} value $J_{56} = -1.9$ cm^{-1} (Table 3), which is

within experimental error of zero. Note also that the whole molecule behaves, at low T, as two Fe_2 pairs separated by a diamagnetic Fe_8 'bridge', so the J_{MSC} couplings between Fe_2 pairs and Fe_8 ions are moot (Figure 8).

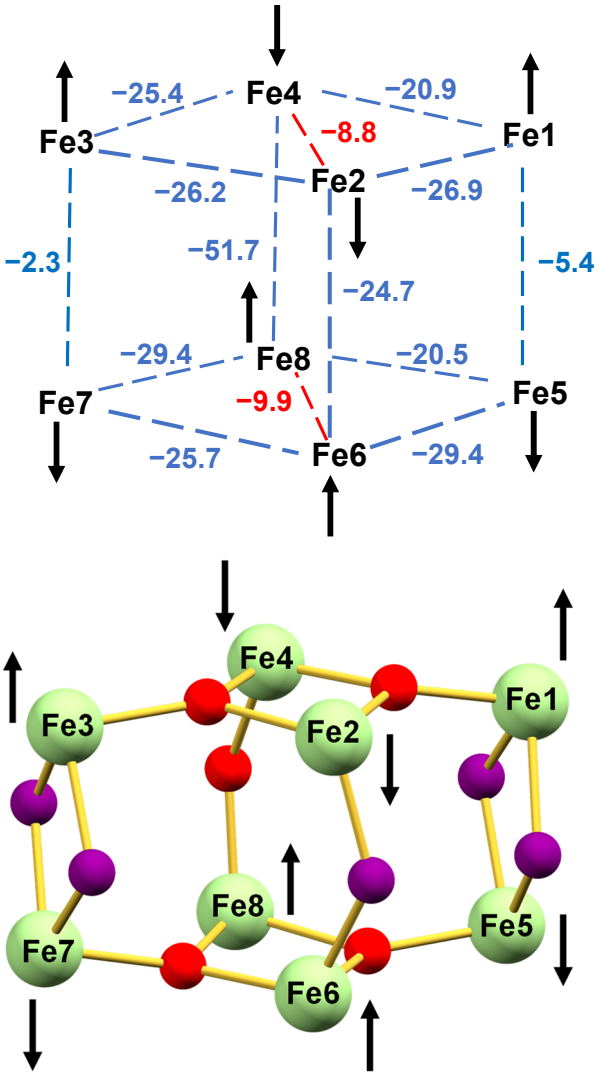

Figure 7. (**top**) Calculated J_{MSC} from Table 3 and the predicted spin vector alignments for the anion of **1**. Frustrated and satisfied J_{MSC} are shown in red and blue, respectively. (**bottom**) Spin vector alignments on the core to emphasize the bridging oxo positions.

The J_{MSC} and J_{DFT} for **3** are overall in satisfying agreement (Table 3) and thus provide independent support for each other. For both, the J_{bb} are stronger than those for **2**, and we assign this to an even bigger effect of the La^{3+} on the Fe_8 structural parameters than the Ca^{2+}. For example, the average wingtip Fe-μ_3-O^{2-} lengths are 1.924 Å, 1.853 Å, and 1.845 Å in **1**–**3**, respectively, and although those for **2** and **3** are similar, their average body Fe-μ_3-O^{2-} lengths are very different at 1.958 Å and 1.908 Å, respectively, rationalizing the stronger couplings in **3**. The central Fe_8 of **3** should again have an $S = 0$ local ground state (Figure 9), whereas as for **2**, the overall ground state is again determined by the intra-Fe_2 coupling within Fe_2 pairs (Fe1Fe6) at each end, for which J_{MSC} and J_{DFT} values are very weakly **AF** (−3.7 and −0.1 cm^{-1}). However, both the dc and ac data clearly indicate their coupling to be **F**, resulting in $S = 5$ ground states for both pairs, and showing that their **AF** J_{MSC} and J_{DFT} values must be artifacts of the very small numbers involved and their inherent uncertainties.

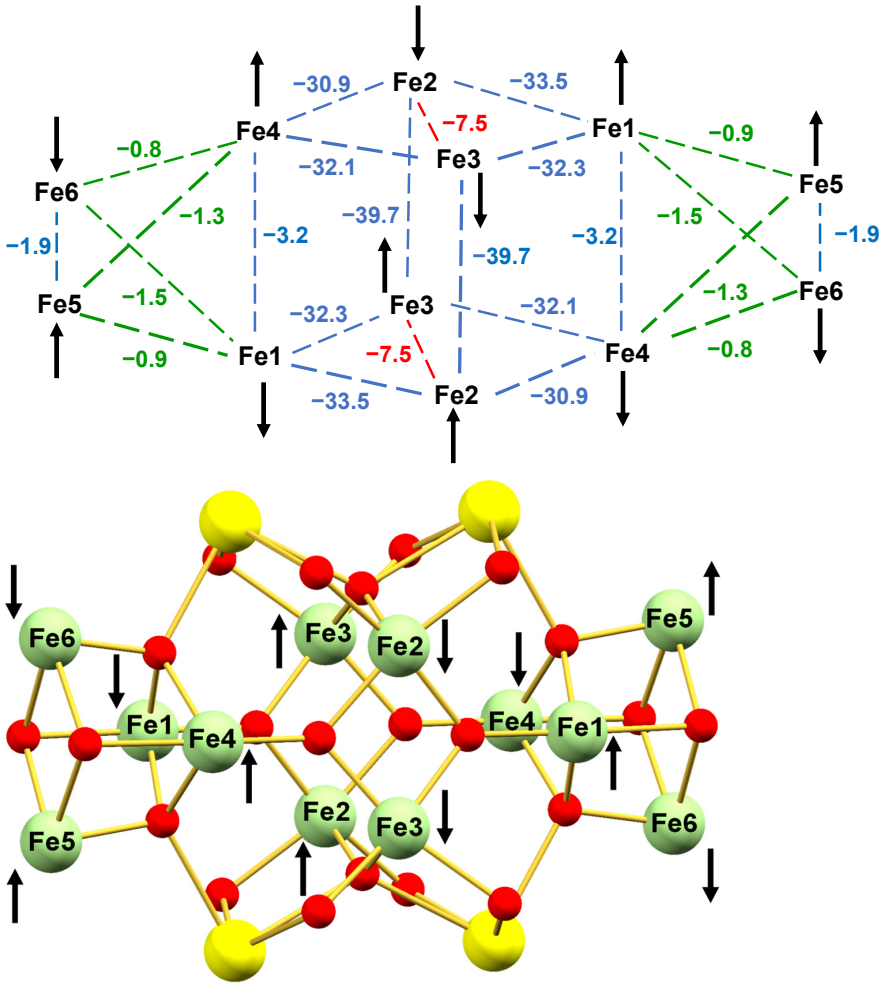

Figure 8. (**top**) Calculated J_{MSC} from Table 3 and the predicted spin vector alignments for **2**. Frustrated and satisfied J_{MSC} are shown in red and blue, respectively; green interactions are moot at low T due to the central Fe_8 being in its local $S = 0$ ground state (**bottom**) Spin vector alignments shown on the core to emphasize the bridging oxo positions. In both figures, the relative spin vector alignments at Fe5 and Fe6 are arbitrary.

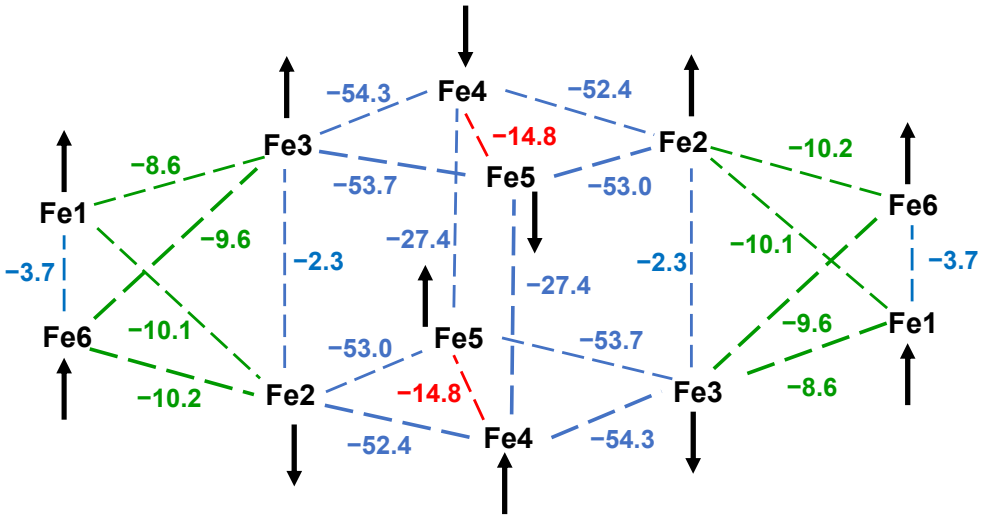

Figure 9. *Cont.*

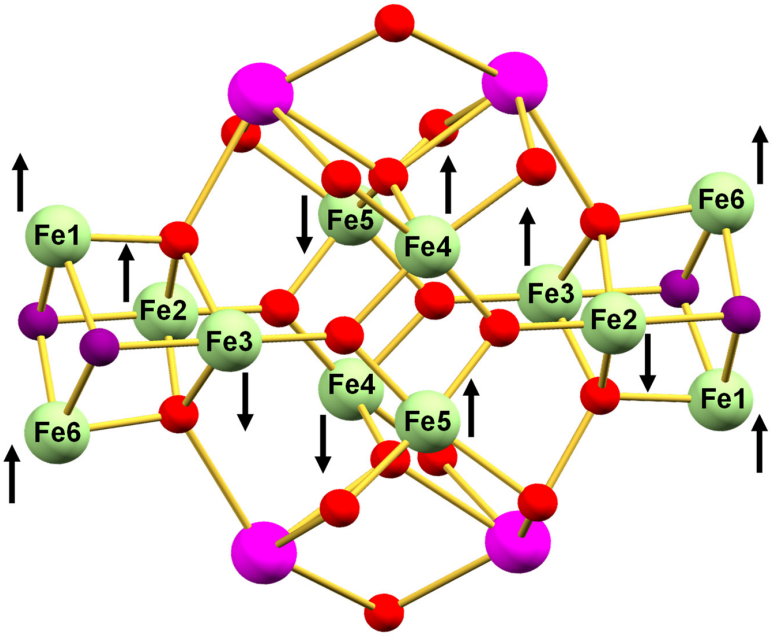

Figure 9. (**top**) Calculated J_{MSC} from Table 3 and the predicted spin vector alignments for **3**. Frustrated and satisfied J_{MSC} are shown in red and blue, respectively; green interactions are moot at low T due to the central Fe_8 being in its local S = 0 ground state. (**bottom**) Spin vector alignments shown on the core to emphasize the bridging oxo positions.

There is still one unexpected experimental observation that needs to be resolved. At low T, **3** can be described as two S = 5 Fe_2 pairs separated by a large diamagnetic Fe_8 unit, and the inter-Fe_2 interaction within each molecule of **3** should therefore be zero and the $\chi_M T$ should be ~30.0 cm^3 K mol^{-1}, the spin-only value for two independent S = 5 units. As stated earlier, however, it is instead 39.01 cm^3 K mol^{-1} at 8.0 K, significantly greater than expected. After close examination of the crystal packing, we assign this to inter-Fe_2 interactions between adjacent molecules of **3**, i.e., intermolecular interactions.

The packing shows that 4-^{t}Bu-benzoate groups on one molecule of **3** lie essentially perpendicular to those on the adjacent molecule, and this is true for all the nearest-neighbours of a particular molecule. One such pair of molecules showing two of the near-perpendicular pairs of ligands is shown in Figure 10. Since it is well known that significant π-spin density will delocalize from metal d_π orbitals to the *para*-position of an aromatic ligand, such as benzoate through a π-spin-delocalization mechanism, and then onto any *para*-substituent with available π-symmetry atomic or molecular orbitals, such as CH_3, CR_3, Cl, F, etc, then the fact that the two π-systems on the different molecules are near-perpendicular should lead to them being orthogonal and thus provide a resulting **F** interaction. Its magnitude is expected to be very weak, but since there is a 3D network of such interactions, it should lead to an overall significant contribution to $\chi_M T$ at low T, and this would rationalize the unexpectedly high observed value. Crucially, there are no π-π-stacking interactions between phenyl groups, common in unsubstituted benzoate complexes, that would be expected to provide **AF** interactions, the bulky *para*-^{t}Bu groups preventing close approach of the aromatic rings in **3**. Support for the above rationalization includes the intermolecular **F** interactions seen for a Mn_4 complex with 4-*tert*-butyl-salicylidene-2-ethanolamine ligation, whose ^{t}Bu-substituted aromatic ligands are also near-perpendicular [103]. Previously reported compounds containing $Fe_{12}Ln_4$ with aromatic ligands also have exhibited unusually high values of $\chi_M T$ at low temperatures, consistent with the observation of intermolecular **F** interactions for such compounds [54,55].

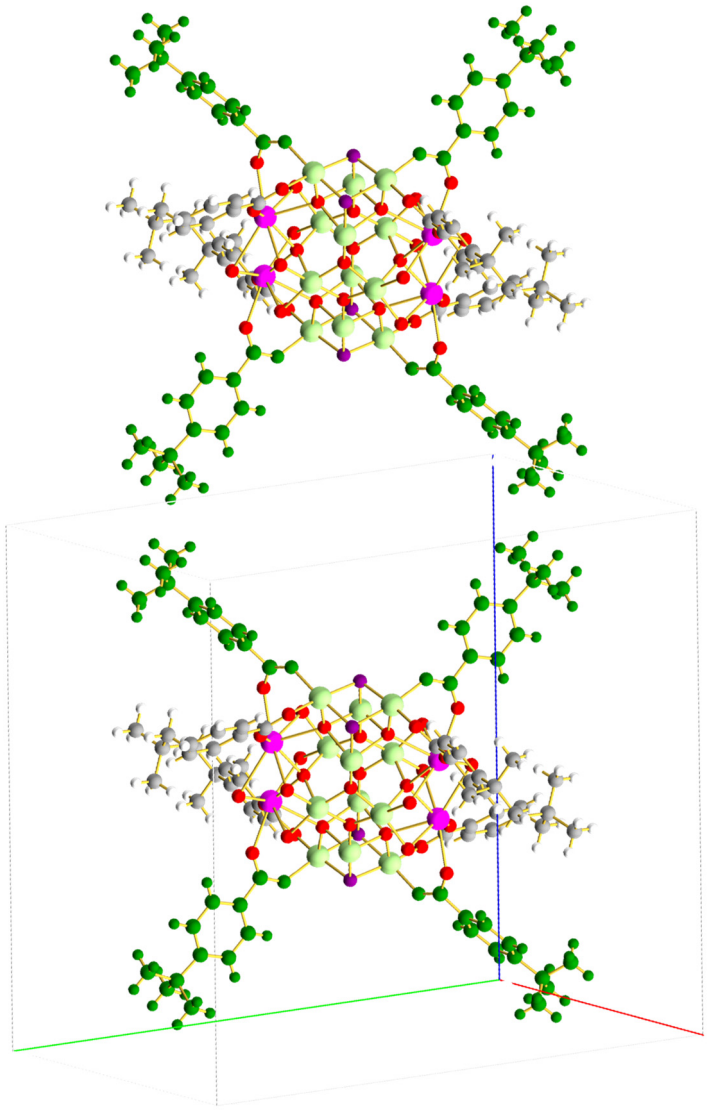

Figure 10. Two adjacent molecules of **3** in the crystal showing two pairs of near-perpendicular 4-^{t}Bu-benzoate ligands (all green) between them. Other colours: Fe^{3+} light green, La^{3+} magneta, O red, OH^{-} purple, C grey, and H white. Some C and H atoms were omitted for clarity. Ligands in dark green are to highlight the interaction pathway.

4. Conclusions

The attainment of a family of three structurally related complexes **1**–**3** has allowed comparisons and contrasts of their observed magnetic properties and yielded important insights into their origin, including those that at first glance appear surprising, and the effect of the attachment of heterometals Ca^{2+} and La^{3+}. The presence of spin frustration and its importance in determining the ground states of polynuclear complexes is yet again emphasized, as is the usefulness of a multi-pronged approach to their analysis using experimental data in coordination with estimates of the constituent J_{ij} exchange couplings, using DFT computations and a magnetostructural correlation derived specifically for Fe^{III}-oxo clusters.

Supplementary Materials: The following supporting information can be downloaded at: https://www.mdpi.com/article/10.3390/chemistry5030110/s1, Figures S1–S3: Stereopair of the complete anion of **1**, complex **2** and complex **3,** respectively; Figure S4: Expanded version of Figure 10 showing the near-perpendicular alignment of 4-tBu-benzoate ligands for four molecules of **3**. The a axis is the red line, b axis is the lime green line, and the c axis is the blue line; Figures S5–S7: Infrared spectrum of **1**, **2**, and **3,** respectively; Table S1: Bond valence sums and assignments for the Fe atoms in the asymmetric unit of **1**; Table S2: Bond valence sums and assignments for O atoms in the cation of **1**; Table S3: Bond valence sums and assignments for the Fe and O atoms in the asymmetric unit of **2**; Table S4: Bond valence sums and assignments for the Fe and O atoms in the asymmetric unit of **3**; Table S5: RMSD calculations for **1** with **2**; Table S6: RMSD calculations for **1** with **3.** CCDC 2276564 contains supplementary crystallographic data for **1**. CCDC 2276685 contains supplementary crystallographic data for **2**. CCDC 2276660 contains supplementary crystallographic data for **3**.

Author Contributions: Conceptualization, G.C.; methodology, A.P.S., C.L.B. and K.H.K.L.; software, A.P.S., C.L.B., K.H.K.L. and J.E.P.; validation, G.C.; formal analysis, A.P.S., C.L.B., K.H.K.L. and K.A.A.; investigation, C.L.B., A.P.S. and K.H.K.L.; resources, G.C. and J.E.P.; data curation, J.E.P., A.P.S., C.L.B., K.A.A. and K.H.K.L.; writing—original draft preparation, A.P.S., C.L.B. and K.H.K.L.; writing—review and editing, G.C., A.P.S., C.L.B. and K.H.K.L.; visualization, K.A.A., C.L.B. and K.H.K.L.; supervision, G.C.; project administration, G.C.; funding acquisition, G.C. All authors have read and agreed to the published version of the manuscript.

Funding: This work was supported by the U.S. National Science Foundation (Grant CHE-1900321), and by the Department of Energy, Office of Science, Office of Basic Energy Sciences, as part of the Computational Chemical Sciences Program under Award #DE-SC0018331. We thank the U.S. National Science Foundation for funding of the X-ray diffractometer at the University of Florida through grant CHE-1828064.

Institutional Review Board Statement: Not applicable.

Informed Consent Statement: Not applicable.

Data Availability Statement: The crystallographic data can be obtained free of charge via http://www.ccdc.cam.ac.uk/conts/retrieving.html (accessed on 30 June 2023), or from the Cambridge Crystallographic Data Centre, 12 Union Road, Cambridge CB2 1EZ, UK; fax: (+44) 1223-336-033; or e-mail: deposit@ccdc.cam.ac.uk.

Conflicts of Interest: The authors declare that they have no known competing financial interests or personal relationships that could have appeared to influence the work reported in this paper.

References

1. Bagai, R.; Christou, G. The Drosophila of single-molecule magnetism: $Mn_{12}O_{12}(O_2CR)_{16}(H_2O)_4$. *Chem. Soc. Rev.* **2009**, *38*, 1011–1026. [CrossRef] [PubMed]
2. Brimblecombe, R.; Swiegers, G.F.; Dismukes, G.C.; Spiccia, L. Sustained water oxidation photocatalysis by a bioinspired manganese cluster. *Angew. Chem. Int. Ed. Engl.* **2008**, *47*, 7335–7338. [CrossRef]
3. Maayan, G.; Gluz, N.; Christou, G. A bioinspired soluble manganese cluster as a water oxidation electrocatalyst with low overpotential. *Nat. Cat.* **2018**, *1*, 48–54. [CrossRef]
4. Chakraborty, R.; Das Kumar, B. Cobalt(III)-oxo cubane clusters as catalysts for oxidation of organic substrates. *J. Chem. Sci.* **2011**, *123*, 163–173.
5. Vincent, J.B.; Huffman, J.C.; Christou, G.; Li, Q.; Nanny, M.A.; Hendrickson, D.N.; Fong, R.H.; Fish, R.H. Modeling the dinuclear sites of iron biomolecules: Synthesis and properties of $Fe_2O(OAc)_2Cl_2(bipy)_2$ and its use as an alkane activation catalyst. *J. Am. Chem. Soc.* **1988**, *110*, 6898–6900. [CrossRef]
6. Seddon, E.J.; Yoo, J.; Folting, K.; Huffman, J.C.; Hendrickson, D.N.; Christou, G. Dinuclear and hexanuclear iron(III) carboxylate clusters with a bis(bipyridine) ligand: Supramolecular aggregation of $[Fe_2O_2]$ units to give a $[Fe_6O_6]$ ladder structure. *J. Chem. Soc. Dalton Trans.* **2000**, 3640–3648. [CrossRef]
7. Grant, C.M.; Knapp, M.J.; Streib, W.E.; Huffman, J.C.; Hendrickson, D.N.; Christou, G. Dinuclear and Hexanuclear Iron(III) Oxide Complexes with a Bis(bipyridine) Ligand: A New $[Fe_6(\mu_3\text{-}O)_4]^{10+}$ Core. *Inorg. Chem.* **1998**, *37*, 6065–6070. [CrossRef]
8. Zheng, H.; Yoo, S.J.; Münck, E.; Que, L. The Flexible $Fe_2(\mu\text{-}O)_2$ Diamond Core: A Terminal Iron(IV)−Oxo Species Generated from the Oxidation of a Bis(μ-oxo)diiron(III) Complex. *J. Am. Chem. Soc.* **2000**, *122*, 3789–3790. [CrossRef]
9. Zang, Y.; Dong, Y.; Que, L.; Kauffmann, K.; Muenck, E. The First Bis(.mu.-oxo)diiron(III) Complex. Structure and Magnetic Properties of $[Fe_2(\mu\text{-}O)_2(6TLA)_2](ClO_4)$. *J. Am. Chem. Soc.* **1995**, *117*, 1169–1170. [CrossRef]

10. Boudalis, A.K.; Raptopoulou, C.P.; Terzis, A.; Perlepes, S.P. 2,2′-Bipyrimidine (bpym) in iron(III) carboxylate chemistry: Preparation and characterization of $[Fe_2O(O_2CMe)_2$ $(bpym)_2(H_2O)_2](ClO_4)_2$, and the influence of weak interactions in the formation of metal clusters. *Polyhedron* **2004**, *23*, 1271–1277. [CrossRef]
11. Zhang, H.-T.; Su, X.-J.; Xie, F.; Liao, R.-Z.; Zhang, M.-T. Iron-Catalyzed Water Oxidation: O–O Bond Formation via Intramolecular Oxo–Oxo Interaction. *Angew. Chem. Int. Ed.* **2021**, *60*, 12467–12474. [CrossRef] [PubMed]
12. Zhang, Z.-M.; Yao, S.; Li, Y.-G.; Clérac, R.; Lu, Y.; Su, Z.-M.; Wang, E.-B. Protein-Sized Chiral Fe_{168} Cages with NbO-Type Topology. *J. Am. Chem. Soc.* **2009**, *131*, 14600–14601. [CrossRef] [PubMed]
13. Hale, A.R.; Lott, M.E.; Peralta, J.E.; Foguet-Albiol, D.; Abboud, K.A.; Christou, G. Magnetic Properties of High-Nuclearity Fex-oxo (x = 7, 22, 24) Clusters Analyzed by a Multipronged Experimental, Computational, and Magnetostructural Correlation Approach. *Inorg. Chem.* **2022**, *61*, 11261–11276. [CrossRef]
14. Herold, S.; Lippard, S.J. Carboxylate-bridged diiron(II) complexes: Synthesis characterization, and O_2-reactivity of models for the reduced diiron centers in methane monooxygenase and ribonucleotide reductase. *J. Am. Chem. Soc.* **1997**, *119*, 145–156. [CrossRef]
15. Lee, D.; Lippard, S.J. Structural and functional models of the dioxygen-activating centers of non-heme diiron enzymes ribonucleotide reductase and soluble methane monooxygenase. *J. Am. Chem. Soc.* **1998**, *120*, 12153–12154. [CrossRef]
16. Menage, S.; Zang, Y.; Hendrich, M.P.; Que, L. Structure and reactivity of a bis(.mu.-acetato-O,O′)diiron(II) complex, $[Fe_2(O_2CCH_3)_2(TPA)_2](BPh_4)_2$. A model for the diferrous core of ribonucleotide reductase. *J. Am. Chem. Soc.* **1992**, *114*, 7786–7792. [CrossRef]
17. Kodera, M.; Itoh, M.; Kano, K.; Funabiki, T.; Reglier, M. A Diiron Center Stabilized by a Bis-TPA Ligand as a Model of Soluble Methane Monooxygenase: Predominant Alkene Epoxidation with H_2O_2. *Angew. Chem. Int. Ed.* **2005**, *44*, 7104–7106. [CrossRef]
18. Xue, G.; Wang, D.; De Hont, R.; Fiedler, A.T.; Shan, X.; Münck, E.; Que, L. A synthetic precedent for the $[Fe^{IV}{}_2(\mu\text{-}O)_2]$ diamond core proposed for methane monooxygenase intermediate Q. *Proc. Nat. Acad. Sci. USA* **2007**, *104*, 20713–20718. [CrossRef]
19. Costas, M.; Rohde, J.U.; Stubna, A.; Ho, R.Y.N.; Quaroni, L.; Münck, E.; Que, L., Jr. A synthetic model for the putative FeIV2O2 diamond core of methane monooxygenase intermediate Q. *J. Am. Chem. Soc.* **2001**, *123*, 12931–12932. [CrossRef]
20. Sankaralingam, M.; Palaniandavar, M. Diiron(III) complexes of tridentate 3N ligands as functional models for methane monooxygenases: Effect of the capping ligand on hydroxylation of alkanes. *Polyhedron* **2014**, *67*, 171–180. [CrossRef]
21. Arii, H.; Nagatomo, S.; Kitagawa, T.; Miwa, T.; Jitsukawa, K.; Einaga, H.; Masuda, H. A novel diiron complex as a functional model for hemerythrin. *J. Inorg. Biochem.* **2000**, *82*, 153–162. [CrossRef]
22. Mizoguchi, T.J.; Kuzelka, J.; Spingler, B.; DuBois, J.L.; Davydov, R.M.; Hedman, B.; Hodgson, K.O.; Lippard, S.J. Synthesis and spectroscopic studies of non-heme diiron(III) species with a terminal hydroperoxide ligand: Models for hemerythrin. *Inorg. Chem.* **2001**, *40*, 4662–4673. [CrossRef] [PubMed]
23. He, C.; Mishina, Y. Modeling non-heme iron proteins. *Curr. Opin. Chem. Biol.* **2004**, *8*, 201–208. [CrossRef] [PubMed]
24. Tshuva, E.Y.; Lippard, S.J. Synthetic Models for Non-Heme Carboxylate-Bridged Diiron Metalloproteins: Strategies and Tactics. *Chem. Rev.* **2004**, *104*, 987–1012. [CrossRef] [PubMed]
25. Que, L. The Road to Non-Heme Oxoferryls and Beyond. *Acc. Chem. Res.* **2007**, *40*, 493–500. [CrossRef]
26. Zhang, X.; Furutachi, H.; Fujinami, S.; Nagatomo, S.; Maeda, Y.; Watanabe, Y.; Kitagawa, T.; Suzuki, M. Structural and Spectroscopic Characterization of (μ-Hydroxo or μ-Oxo)(μ-peroxo)diiron(III) Complexes: Models for Peroxo Intermediates of Non-Heme Diiron Proteins. *J. Am. Chem. Soc.* **2005**, *127*, 826–827. [CrossRef] [PubMed]
27. Foguet-Albiol, D.; Abboud, K.A.; Christou, G. High-nuclearity homometallic iron and nickel clusters: Fe_{22} and Ni_{24} complexes from the use of N-methyldiethanolamine. *Chem. Commun.* **2005**, 4282–4284. [CrossRef]
28. McCusker, J.K.; Vincent, J.B.; Schmitt, E.A.; Mino, M.L.; Shin, K.; Coggin, D.K.; Hagen, P.M.; Huffman, J.C.; Christou, G.; Hendrickson, D.N. Molecular spin frustration in the $[Fe_4O_2]^{8+}$ core: Synthesis, structure, and magnetochemistry of tetranuclear iron-oxo complex $[Fe_4O_2(O_2CR)_7(bpy)_2](C1O_4)$ (R = Me, Ph). *J. Am. Chem. Soc.* **1991**, *113*, 3012–3021. [CrossRef]
29. Kahn, O. Competing spin interactions and degenerate frustration for discrete molecular species. *Chem. Phys. Lett.* **1997**, *265*, 109–114. [CrossRef]
30. Gatteschi, D.; Caneschi, A.; Sessoli, R.; Cornia, A. Magnetism of large iron-oxo clusters. *Chem. Soc. Rev.* **1996**, *25*, 101–109. [CrossRef]
31. Murch, B.P.; Boyle, P.D.; Que, L. Structures of binuclear and tetranuclear iron(III) complexes as models for ferritin core formation. *J. Am. Chem. Soc.* **1985**, *107*, 6728–6729. [CrossRef]
32. Mansour, A.N.; Thompson, C.; Theil, E.C.; Chasteen, N.D.; Sayers, D.E. Fe(III).ATP complexes. Models for ferritin and other polynuclear iron complexes with phosphate. *J. Bio. Chem.* **1985**, *260*, 7975–7979. [CrossRef]
33. Islam, Q.T.; Sayers, D.E.; Theil, E.C.; Gorun, S.M. A comparison of an undecairon(III) complex with the ferritin iron core. *J. Inorg. Biochem.* **1989**, *36*, 51–62. [CrossRef] [PubMed]
34. Taft, K.L.; Papaefthymiou, G.C.; Lippard, S.J. Synthesis, Structure, and Electronic Properties of a Mixed-Valent Dodecairon Oxo Complex, a Model for the Biomineralization of Ferritin. *Inorg. Chem.* **1994**, *33*, 1510–1520. [CrossRef]
35. Lachicotte, R.J.; Hagen, K.S. Synthesis and structures of trinuclear and μ-hydroxo pentanuclear iron(II) carboxylates as models of reduced ferritin and white rust. *Inorg. Chimi. Acta* **1997**, *263*, 407–414. [CrossRef]
36. Taguchi, T.; Thompson, M.S.; Abboud, K.A.; Christou, G. Unusual Fe_9 and Fe_{18} structural types from the use of 2,6-pyridinedimethanol in FeIII cluster chemistry. *Dalton Trans.* **2010**, *39*, 9131–9139. [CrossRef]

37. Gass, I.A.; Milios, C.J.; Evangelisti, M.; Heath, S.L.; Collison, D.; Parsons, S.; Brechin, E.K. Synthesis and magnetic properties of heptadecametallic Fe(III) clusters. *Polyhedron* **2007**, *26*, 1835–1837. [CrossRef]
38. Canada-Vilalta, C.; O'Brien, T.A.; Brechin, E.K.; Pink, M.; Davidson, E.R.; Christou, G. Large spin differences in structurally related Fe_6 molecular clusters and their magnetostructural explanation. *Inorg. Chem.* **2004**, *43*, 5505–5521. [CrossRef]
39. Singh, A.P.; Joshi, R.P.; Abboud, K.A.; Peralta, J.E.; Christou, G. Molecular spin frustration in mixed-chelate Fe_5 and Fe_6 oxo clusters with high ground state spin values. *Polyhedron* **2020**, *176*, 114182. [CrossRef]
40. King, P.; Stamatatos, T.C.; Abboud, K.A.; Christou, G. Reversible Size Modification of Iron and Gallium Molecular Wheels: A Ga10 "Gallic Wheel" and Large Ga_{18} and Fe_{18} Wheels. *Angew. Chem. Int. Ed.* **2006**, *45*, 7379–7383. [CrossRef]
41. Artus, P.; Boskovic, C.; Yoo, J.; Streib, W.E.; Brunel, L.C.; Hendrickson, D.N.; Christou, G. Single-molecule magnets: Site-specific ligand abstraction from $[Mn_{12}O_{12}(O_2CR)_{16}(H_2O)_4]$ and the preparation and properties of $[Mn_{12}O_{12}(NO_3)_4(O_2CCH_2Bu(t))_{12}(H_2O)_4]$. *Inorg. Chem.* **2001**, *40*, 4199–4210. [CrossRef] [PubMed]
42. Boskovic, C.; Pink, M.; Huffman, J.C.; Hendrickson, D.N.; Christou, G. Single-molecule magnets: Ligand-induced core distortion and multiple Jahn-Teller isomerism in $Mn_{12}O_{12}(O_2CMe)_8(O_2PPh_2)_8(H_2O)_4$. *J. Am. Chem. Soc.* **2001**, *123*, 9914–9915. [CrossRef]
43. Brockman, J.T.; Abboud, K.A.; Hendrickson, D.N.; Christou, G. A new family of Mn_{12} single-molecule magnets: Replacement of carboxylate ligands with diphenylphosphinates. *Polyhedron* **2003**, *22*, 1765–1769. [CrossRef]
44. Chakov, N.E.; Abboud, K.A.; Zakharov, L.N.; Rheingold, A.L.; Hendrickson, D.N.; Christou, G. Reaction of $Mn_{12}O_{12}(O_2CR)_{16}(H_2O)_4$ single-molecule magnets with non-carboxylate ligands. *Polyhedron* **2003**, *22*, 1759–1763. [CrossRef]
45. Chakov, N.E.; Wernsdorfer, W.; Abboud, K.A.; Hendrickson, D.N.; Christou, G. Single-molecule magnets. A Mn_{12} complex with mixed carboxylate-sulfonate ligation: $Mn_{12}O_{12}(O_2CMe)_8(O_3SPh)_8(H_2O)_4$. *Dalt. Trans.* **2003**, 2243–2248. [CrossRef]
46. Chakov, N.E.; Wernsdorfer, W.; Abboud, K.A.; Christou, G. Mixed-valence (MnMnIV)-Mn-III clusters $Mn_7O_8(O_2SePh)_8(O_2CMe)(H_2O)$ and $Mn_7O_8(O_2SePh)_9(H_2O)$: Single-chain magnets exhibiting quantum tunneling of magnetization. *Inorg. Chem.* **2004**, *43*, 5919–5930. [CrossRef]
47. Chakov, N.E.; Thuijs, A.E.; Wernsdorfer, W.; Rheingold, A.L.; Abboud, K.A.; Christou, G. Unusual $Mn(III/IV)_4$ Cubane and $Mn^{III}{}_{16}M_4$ (M = Ca, Sr) Looplike Clusters from the Use of Dimethylarsinic Acid. *Inorg. Chem.* **2016**, *55*, 8468–8477. [CrossRef]
48. Konar, S.; Clearfield, A. Synthesis and Characterization of High Nuclearity Iron(III) Phosphonate Molecular Clusters. *Inorg. Chem.* **2008**, *47*, 5573–5579. [CrossRef]
49. Yao, H.-C.; Li, Y.-Z.; Zheng, L.-M.; Xin, X.-Q. Syntheses, structures and magnetic properties of tetra- and heptanuclear iron(III) clusters incorporating phosphonate ligands. *Inorg. Chim. Acta* **2005**, *358*, 2523–2529. [CrossRef]
50. Tolis, E.I.; Helliwell, M.; Langley, S.; Raftery, J.; Winpenny, R.E.P. Synthesis and Characterization of Iron(III) Phosphonate Cage Complexes. *Angew. Chem. Int. Ed.* **2003**, *42*, 3804–3808. [CrossRef]
51. Lee, K.H.K.; Peralta, J.E.; Abboud, K.A.; Christou, G. Iron(III)–Oxo Cluster Chemistry with Dimethylarsinate Ligands: Structures, Magnetic Properties, and Computational Studies. *Inorg. Chem.* **2020**, *59*, 18090–18101. [CrossRef] [PubMed]
52. Lee, K.H.K.; Aebersold, L.; Peralta, J.E.; Abboud, K.A.; Christou, G. Synthesis, Structure, and Magnetic Properties of an Fe_{36} Dimethylarsinate Cluster: The Largest "Ferric Wheel". *Inorg. Chem.* **2022**, *61*, 17256–17267. [CrossRef]
53. Carson, I.; Healy, M.R.; Doidge, E.D.; Love, J.B.; Morrison, C.A.; Tasker, P.A. Metal-binding motifs of alkyl and aryl phosphinates; versatile mono and polynucleating ligands. *Coord. Chem. Rev.* **2017**, *335*, 150–171. [CrossRef]
54. Zeng, Y.F.; Xu, G.C.; Hu, X.; Chen, Z.; Bu, X.H.; Gao, S.; Sanudo, E.C. Single-Molecule-Magnet Behavior in a $Fe_{12}Sm_4$ Cluster. *Inorg. Chem.* **2010**, *49*, 9734–9736. [CrossRef]
55. Liu, S.J.; Zeng, Y.F.; Xue, L.; Han, S.D.; Jia, J.M.; Hu, T.L.; Bu, X.H. Tuning the magnetic behaviors in $Fe^{III}{}_{12}Ln^{III}{}_4$ clusters with aromatic carboxylate ligands. *Inorg. Chem. Front.* **2014**, *1*, 200–206. [CrossRef]
56. Zheng, X.Y.; Zhang, H.; Wang, Z.X.; Liu, P.X.; Du, M.H.; Han, Y.Z.; Wei, R.J.; Ouyang, Z.W.; Kong, X.J.; Zhuang, G.L.; et al. Insights into Magnetic Interactions in a Monodisperse $Gd_{12}Fe_{14}$ Metal Cluster. *Angew. Chem.-Int. Ed.* **2017**, *56*, 11475–11479. [CrossRef]
57. Zheng, X.Y.; Du, M.H.; Amiri, M.; Nyman, M.; Liu, Q.; Liu, T.; Kong, X.J.; Long, L.S.; Zheng, L.S. Atomically Precise Lanthanide-Iron-Oxo Clusters Featuring the epsilon-Keggin Ion. *Chem. Eur. J.* **2020**, *26*, 1388–1395. [CrossRef] [PubMed]
58. Zheng, X.Y.; Chen, M.T.; Du, M.H.; Wei, R.J.; Kong, X.J.; Long, L.S.; Zheng, L.S. Capturing Lacunary Iron-Oxo Keggin Clusters and Insight Into the Keggin-Fe-13 Cluster Rotational Isomerization. *Chem. Eur. J.* **2020**, *26*, 11985–11988. [CrossRef]
59. Koumousi, E.S.; Mukherjee, S.; Beavers, C.M.; Teat, S.J.; Christou, G.; Stamatatos, T.C. Towards models of the oxygen-evolving complex (OEC) of photosystem II: A Mn_4Ca cluster of relevance to low oxidation states of the OEC. *Chem. Comm.* **2011**, *47*, 11128–11130. [CrossRef]
60. Alaimo, A.A.; Takahashi, D.; Cunha-Silva, L.; Christou, G.; Stamatatos, T.C. Emissive $\{Mn^{III}{}_4Ca\}$ Clusters with Square Pyramidal Topologies: Syntheses and Structural, Spectroscopic, and Physicochemical Characterization. *Inorg. Chem.* **2015**, *54*, 2137–2151. [CrossRef]
61. Mukherjee, S.; Stull, J.A.; Yano, J.; Stamatatos, T.C.; Pringouri, K.; Stich, T.A.; Abboud, K.A.; Britt, R.D.; Yachandra, V.K.; Christou, G. Synthetic model of the asymmetric $[Mn_3CaO_4]$ cubane core of the oxygen-evolving complex of photosystem II. *Proc. Nat. Acad. Sci. USA* **2012**, *109*, 2257–2262. [CrossRef] [PubMed]
62. Coleman, J.E. Structure and mechanism of alkaline phosphatase. *Annu. Rev. Biophys. Biomol. Struct.* **1992**, *21*, 441–483. [CrossRef] [PubMed]
63. Lassila, J.K.; Zalatan, J.G.; Herschlag, D. Biological phosphoryl-transfer reactions: Understanding mechanism and catalysis. *Annu. Rev. Biochem.* **2011**, *80*, 669–702. [CrossRef] [PubMed]

64. Kamerlin, S.C.; Sharma, P.K.; Prasad, R.B.; Warshel, A. Why nature really chose phosphate. *Q. Rev. Biophys.* **2013**, *46*, 1–132. [CrossRef]
65. Yong, S.C.; Roversi, P.; Lillington, J.; Rodriguez, F.; Krehenbrink, M.; Zeldin, O.B.; Garman, E.F.; Lea, S.M.; Berks, B.C. A complex iron-calcium cofactor catalyzing phosphotransfer chemistry. *Science* **2014**, *345*, 1170–1173. [CrossRef]
66. Herbert, D.E.; Lionetti, D.; Rittle, J.; Agapie, T. Heterometallic Triiron-Oxo/Hydroxo Clusters: Effect of Redox-Inactive Metals. *J. Am. Chem. Soc.* **2013**, *135*, 19075–19078. [CrossRef]
67. Prodius, D.; Turta, C.; Mereacre, V.; Shova, S.; Gdaniec, M.; Simonov, Y.; Lipkowski, J.; Kuncser, V.; Filoti, G.; Caneschi, A. Synthesis, structure and properties of heterotrinuclear carboxylate complexes $[Fe_2M(Ca, Sr, Ba)O(CCl_3COO)_6(THF)_n]$. *Polyhedron* **2006**, *25*, 2175–2182. [CrossRef]
68. Burger, J.; Klüfers, P. Stabilization of Iron Clusters by Polyolato Ligands and Calcium Ions: An Fe_{14} Oxocluster from Aqueous Alkaline Solution. *Angew. Chem. Int. Ed.* **1997**, *36*, 776–779. [CrossRef]
69. Prakash, R.; Saalfrank, R.W.; Maid, H.; Scheurer, A.; Heinemann, F.W.; Trautwein, A.X.; Böttger, L.H. Synthesis and Redox Properties of Mixed-Valent Octanuclear Iron Defective Hexacubanes and a (CaCl)-Capped Body-Centered Six-Sided Iron(III) Polyhedron. *Angew. Chem. Int. Ed.* **2006**, *45*, 5885–5889. [CrossRef]
70. Earnshaw, A.; Figgis, B.N.; Lewis, J. Chemistry of polynuclear compounds. Part VI. Magnetic properties of trimeric chromium and iron carboxylates. *J. Chem. Soc. A* **1966**, 1656–1663. [CrossRef]
71. Sheldrick, G. Crystal structure refinement with SHELXL. *Acta Crystallogr. Sect. C* **2015**, *71*, 3–8. [CrossRef] [PubMed]
72. Spek, A. PLATON SQUEEZE: A tool for the calculation of the disordered solvent contribution to the calculated structure factors. *Acta Cryst. Sec. C* **2015**, *71*, 9–18. [CrossRef] [PubMed]
73. Spek, A. Structure validation in chemical crystallography. *Acta Cryst. Sec. D* **2009**, *65*, 148–155. [CrossRef] [PubMed]
74. Gagne, O.C.; Hawthorne, F.C. Comprehensive derivation of bond-valence parameters for ion pairs involving oxygen. *Acta Cryst. Sec. B Struc. Sci. Cryst. Eng. Mat.* **2015**, *71*, 562–578. [CrossRef] [PubMed]
75. Brown, I.D.; Altermatt, D. Bond-Valence Parameters Obtained from a Systematic Analysis of the Inorganic Crystal-Structure Database. *Acta Cryst. Sec. B Struc. Sci.* **1985**, *41*, 244–247. [CrossRef]
76. Bain, G.A.; Berry, J.F. Diamagnetic corrections and Pascal's constants. *J. Chem. Edu.* **2008**, *85*, 532–536. [CrossRef]
77. Van Wullen, C. Broken Symmetry Approach to Density Functional Calculation of Magnetic Anisotropy or Zero Field Splittings for Multinuclear Complexes with Antiferromagnetic Coupling. *J. Phys. Chem. A* **2009**, *113*, 11535–11540. [CrossRef]
78. Bencini, A.; Totti, F.; Daul, C.A.; Doclo, K.; Fantucci, P.; Barone, V. Density functional calculations of magnetic exchange interactions in polynuclear transition metal complexes. *Inorg. Chem.* **1997**, *36*, 5022–5030. [CrossRef]
79. Ruiz, E.; Rodriguez-Fortea, A.; Cano, J.; Alvarez, S.; Alemany, P. About the calculation of exchange coupling constants in polynuclear transition metal complexes. *J. Comp. Chem.* **2003**, *24*, 982–989. [CrossRef]
80. Valero, R.; Costa, R.; Moreira, I.; Truhlar, D.G.; Illas, F. Performance of the M06 family of exchange-correlation functionals for predicting magnetic coupling in organic and inorganic molecules. *J. Chem. Phys.* **2008**, *128*, 114103. [CrossRef]
81. Comba, P.; Hausberg, S.; Martin, B. Calculation of Exchange Coupling Constants of Transition Metal Complexes with DFT. *J. Phys. Chem.* **2009**, *113*, 6751–6755. [CrossRef] [PubMed]
82. Phillips, J.J.; Peralta, J.E. Magnetic Exchange Couplings from Semilocal Functionals Evaluated Nonself-Consistently on Hybrid Densities: Insights on Relative Importance of Exchange, Correlation, and Delocalization. *J. Chem. Theory Comp.* **2012**, *8*, 3147–3158. [CrossRef]
83. Joshi, R.P.; Phillips, J.J.; Mitchell, K.J.; Christou, G.; Jackson, K.A.; Peralta, J.E. Accuracy of density functional theory methods for the calculation of magnetic exchange couplings in binuclear iron(III) complexes. *Polyhedron* **2020**, *176*, 114194. [CrossRef]
84. Hehre, W.J.; Ditchfield, R.; Pople, J.A. Self-consistent molecular-orbital methods.12. further extensions of gaussian-type basis sets for use in molecular-orbital studies of organic-molecules. *J. Chem. Phys.* **1972**, *56*, 2257. [CrossRef]
85. Krishnan, R.; Binkley, J.S.; Seeger, R.; Pople, J.A. Self-consistent molecular-orbital methods.20. basis set for correlated wave-functions. *J. Chem. Phys.* **1980**, *72*, 650–654. [CrossRef]
86. Blaudeau, J.P.; McGrath, M.P.; Curtiss, L.A.; Radom, L. Extension of Gaussian-2 (G2) theory to molecules containing third-row atoms K and Ca. *J. Chem. Phys.* **1997**, *107*, 5016–5021. [CrossRef]
87. Pantazis, D.A.; Neese, F. All-Electron Scalar Relativistic Basis Sets for the Lanthanides. *J. Chem. Theory Comp.* **2009**, *5*, 2229–2238. [CrossRef]
88. Douglas, M.; Kroll, N.M. Quantum electrodynamical corrections to the fine structure of helium. *Ann. Phys.* **1974**, *82*, 89–155. [CrossRef]
89. Hess, B.A. Applicability of the no-pair equation with free-particle projection operators to atomic and molecular-structure calculations. *Phys. Rev.* **1985**, *32*, 756–763. [CrossRef]
90. Hess, B.A. Relativistic electronic-structure calculations employing a two-component no-pair formalism with external-field projection operators. *Phys. Rev.* **1986**, *33*, 3742–3748. [CrossRef]
91. Frisch, M.J.; Trucks, G.W.; Schlegel, H.B.; Scuseria, G.E.; Robb, M.A.; Cheeseman, J.R.; Scalmani, G.; Barone, V.; Petersson, G.A.; Nakatsuji, H.; et al. Gaussian 16, Revision B.01, Gaussian, Inc.: Wallingford, CT, USA, 2016.
92. Armstrong, W.H.; Roth, M.E.; Lippard, S.J. Tetranuclear iron-oxo complexes. Synthesis, structure, and properties of species containing the nonplanar $\{Fe_4O_2\}^{8+}$ core and seven bridging carboxylate ligands. *J. Am. Chem. Soc.* **1987**, *109*, 6318–6326. [CrossRef]

93. Boudalis, A.K.; Lalioti, N.; Spyroulias, G.A.; Raptopoulou, C.P.; Terzis, A.; Bousseksou, A.; Tangoulis, V.; Tuchagues, J.-P.; Perlepes, S.P. Novel Rectangular $[Fe_4(\mu_4\text{-}OHO)(\mu\text{-}OH)_2]^{7+}$ versus "Butterfly" $[Fe_4(\mu_3\text{-}O)_2]^{8+}$ Core Topology in the Fe^{III}/RCO_2^-/phen Reaction Systems (R = Me, Ph; phen = 1,10-Phenanthroline): Preparation and Properties of $[Fe_4(OHO)(OH)_2(O_2CMe)_4(phen)_4](ClO4)_3$, $[Fe_4O_2(O_2CPh)_7(phen)_2](ClO_4)$, and $[Fe_4O_2(O_2CPh)_8(phen)]$. *Inorg. Chem.* **2002**, *41*, 6474–6487. [CrossRef] [PubMed]
94. Arizaga, L.; Gancheff, J.S.; Faccio, R.; Cañón-Mancisidor, W.; González, R.; Kremer, C.; Chiozzone, R. Synthesis, crystal structure and magnetic properties of a novel tetranuclear oxo-bridged iron(III) butterfly. *J. Mol. Struct.* **2014**, *1058*, 149–154. [CrossRef]
95. Bagai, R.; Abboud, K.A.; Christou, G. A New N,N,O Chelate for Transition Metal Chemistry: Fe_5 and Fe_6 Clusters from the Use of 6-Hydroxymethyl-2,2′-bipyridine (hmbpH). *Inorg. Chem.* **2007**, *46*, 5567–5575. [CrossRef]
96. Bagai, R.; Datta, S.; Betancur-Rodriguez, A.; Abboud, K.A.; Hill, S.; Christou, G. Diversity of New Structural Types in Polynuclear Iron Chemistry with a Tridentate N,N,O Ligand. *Inorg. Chem.* **2007**, *46*, 4535–4547. [CrossRef]
97. Chaudhuri, P.; Winter, M.; Fleischhauer, P.; Haase, W.; Flörke, U.; Haupt, H.-J. Synthesis, structure and magnetism of a tetranuclear Fe(III) complex containing an $[Fe_4(\mu_3\text{-}O)_2]^{8+}$ core. *Inorg. Chim. Acta* **1993**, *212*, 241–249. [CrossRef]
98. Ammala, P.; Cashion, J.D.; Kepert, C.M.; Moubaraki, B.; Murray, K.S.; Spiccia, L.; West, B.O. An Octanuclear Fe^{III} Compound Featuring a New Type of Double Butterfly Iron–Oxo Core. *Angew. Chem. Int. Ed.* **2000**, *39*, 1688–1690. [CrossRef]
99. Cauchy, T.; Ruiz, E.; Alvarez, S. Magnetostructural Correlations in Polynuclear Complexes: The Fe_4 Butterflies. *J. Am. Chem. Soc.* **2006**, *128*, 15722–15727. [CrossRef]
100. Overgaard, J.; Hibbs, D.E.; Rentschler, E.; Timco, G.A.; Larsen, F.K. Experimental and Theoretical Electron Density Distribution and Magnetic Properties of the Butterfly-like Complex $[Fe_4O_2(O_2CCMe_3)_8(NC_5H_4Me)_2]\cdot 2CH_3CN$. *Inorg. Chem.* **2003**, *42*, 7593–7601. [CrossRef]
101. Mitchell, K.J.; Abboud, K.A.; Christou, G. Magnetostructural Correlation for High-Nuclearity Iron(III)/Oxo Complexes and Application to Fe_5, Fe_6, and Fe_8 Clusters. *Inorg. Chem.* **2016**, *55*, 6597–6608. [CrossRef]
102. Hale, A.R.; Aebersold, L.E.; Peralta, J.E.; Foguet-Albiol, D.; Abboud, K.A.; Christou, G. Analysis of spin frustration in an Fe^{III}_7 cluster using a combination of computational, experimental, and magnetostructural correlation methods. *Polyhedron* **2022**, *225*, 116045. [CrossRef]
103. Boskovic, C.; Bircher, R.; Tregenna-Piggott, P.L.W.; Gudel, H.U.; Paulsen, C.; Wernsdorfer, W.; Barra, A.L.; Khatsko, E.; Neels, A.; Stoeckli-Evans, H. Ferromagnetic and antiferromagnetic intermolecular interactions in a new family of Mn_4 complexes with an energy barrier to magnetization reversal. *J. Am. Chem. Soc.* **2003**, *125*, 14046–14058. [CrossRef] [PubMed]